

# Quantitative Approach for the Accurate CFD Simulation of Hover in Turbulent Flow

Neal M. Chaderjian\*

Corresponding author: Neal.Chaderjian@nasa.gov

\*NASA Ames Research Center, Moffett Field, CA, USA

**Abstract:** Time-dependent Navier-Stokes simulations have been carried out for a V22 rotor in hover using an improved, low-diffusion, HLLC++ upwind algorithm in the OVERFLOW code. Emphasis is placed on lessons learned over the past decade regarding the effects of high-order spatial accuracy, grid resolution, and the use of detached eddy simulation in predicting the rotor performance, i.e., figure-of-merit (FM). A quick-start procedure is described together with a statistical measure of FM convergence that reduces hover computations by 5 times, similar in computational work for forward flight. Furthermore, Cartesian adaptive mesh refinement in the rotor wake revealed a complex turbulent flow with worm-like structures of various scales. These turbulent worms, found computationally more than a decade ago, have recently been observed in a separate German Aerospace Center (DLR) experiment. Moreover, adaptive mesh refinement has been used to resolve the tip-vortex to its correct physical size.

*Keywords: Higher-order differences, detached eddy simulation, solution convergence, turbulent wake.*

## 1. Introduction

Helicopters and tiltrotors are two examples of vertical lift vehicles that are commonly used in commercial and military applications due to their ability to take off and land vertically. The former provides excellent hover capability while the latter can carry larger payloads at greater speeds and distances. A new class of vertical lift vehicles has emerged known as Urban Air Mobility (UAM). These vertical take-off and landing (VTOL) or short take-off and landing (STOL) aircraft aim to revolutionize urban aviation by making air transportation more accessible using autonomous systems and by removing the need for traditional airport infrastructure. Moreover, UAM designs are environmentally friendly using quiet and clean electric or hybrid propulsion. These vehicles can transport 4-6 passengers at distances of 100 miles and speeds up to 140 mph. Examples of all three classes of vehicles are shown in Fig. 1.



a) UH-60 Blackhawk helicopter. b) V-22 Osprey tiltrotor. c) JOBY UAM.

**Figure 1** Three examples of rotary wing aircraft.

All of these vehicles rely on rotors as their main source of lift and propulsion, and computational fluid dynamic (CFD) simulations of hover using the Navier-Stokes equations has become an important design

tool in the evaluation of new UAM concepts. The figure-of-merit (FM) is a key hover performance parameter defined as

$$FM = \frac{C_T^{3/2}}{\sqrt{2} C_Q} \quad (1)$$

where  $C_T$  is the thrust coefficient and  $C_Q$  is the torque coefficient. This expression is the ratio of the ideal torque (from inviscid momentum theory) to the actual torque and is a measure of the rotor efficiency.

The accurate CFD prediction of FM is computationally challenging. Spatial accuracy and the turbulence model have a strong effect on CFD prediction accuracy. Moreover, computational cost can be an issue because the initial startup transients of a spinning rotor can take a long time to get established, especially in a closed test facility, e.g., a wind tunnel. This is the fundamental nature of a self-induced low-speed flow. In fact, it is a common practice in an experiment to let the rotor spin a hundred or more revolutions before measuring the forces and moments. On the other hand, a common CFD practice is to run simulations from impulsive start with 10 or fewer revolutions to reduce the computational cost. The FM response begins to look flat after a while but hasn't truly settled out. Small changes over a long time can result in significant changes in the final converged FM.

A 2009 state-of-the-art assessment [1] reported that the average CFD predictive error of FM was 2.4%. It was difficult to determine how much of this discrepancy was due to CFD methodology or experimental measurement technique. The CFD goal of predicting FM with less than 1% error seemed unlikely at the time. Figure 2 provides two examples of the state-of-the-art at that time [2-3], where the FM was typically underpredicted. This is significant because underpredicting FM by 0.005 (about 0.6%) is equivalent to reducing the payload by one passenger. It was thought that poor resolution of the blade-tip vortices was the main cause of this discrepancy. This was later proved to be incorrect [4] but did lead to the development of adaptive mesh refinement (AMR) techniques to better resolve the blade-tip vortices in the rotor wake.

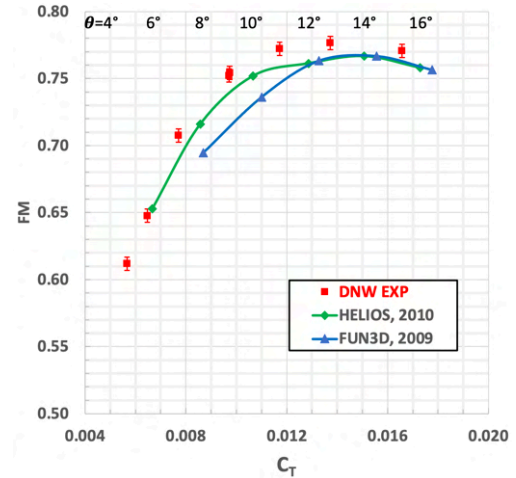


**Figure 2** CFD FM for the  $\frac{1}{4}$ -scale TRAM model, circa 2009-2010 [2-3].

Chaderjian and Buning [4] first demonstrated an order-of-magnitude improvement in predicting the FM for the Tilt Rotor Aeroacoustics Model (TRAM), a  $\frac{1}{4}$ -scale model of the V22 Osprey rotor tested in the DNW wind tunnel [5-6]. These CFD computations agreed with measured FM within 0.2% over a range of collectives ( $\theta$ ). However, a surprising result of this study was the discovery of a complex turbulent wake consisting of large eddy simulation (LES) vortical structures, which were referred to as turbulent worms. This occurred as the wake-grid spacing was refined from a typical value of  $\Delta_{wake}=10\%c_{tip}$  to  $2.5\%c_{tip}$ , where  $c_{tip}$  is the rotor tip chord. Chaderjian [7] later provided a more detailed explanation of the FM improvement and formation of the worm-like structures found in the turbulent wake. This prompted the development of a working group to explore the CFD simulation of hover [8], and since then others have noted a similar turbulent wake with worms when using higher-order spatial accuracy and refined wake meshes [9-11]. However, it took more than a decade to verify experimentally the existence of these turbulent worms using tomographic particle image velocimetry (tomo-PIV) [12].

Considerable progress has been made in predicting the FM over the past decade. The purpose of this paper is to present an approach to reliably predict a rotor's FM in fully turbulent flow. It is recognized that modeling turbulent transition can be important, but this is still a topic of research. Emphasis here will be

placed on temporal and spatial accuracy, the turbulence model, and a statistical approach to quantitatively determine when the hover FM is converged, including how many significant figures are justified to report. A general quick-start procedure will also be presented that reduces the computational cost of a tightly converged hover simulation to that of forward flight, typically about 7 revolutions (revs) from impulsive start. A detailed description of the turbulent rotor wake will be provided, including vortex pairing and breakdown, and the physical process leading to the formation of turbulent worms. Experimental evidence of these worms will also be discussed.

The following sections include a description of the experimental data, numerical approach, results and discussion, and concluding remarks.

## 2. Experimental Data

The numerical results presented in this paper are validated with wind-tunnel measurements of the Tilt Rotor Aeroacoustics Model (TRAM), which is a 1/4-scale wind-tunnel model of the V22 Osprey rotor. This model was constructed and tested to facilitate tiltrotor aeromechanics research, and provides a significant source of aeroacoustic, performance, and structural loads data for validation of tiltrotor analyses. The stiff rotor blades are ideally suited for aerodynamic CFD validation without the additional uncertainty introduced by blade flexibility. The TRAM rotor was tested in the Duits-Nederlandse Windtunnel Large Low-speed Facility (DNW-LLF) in the spring of 1998. Table 1 summarizes the TRAM model geometric characteristics, nominal hover test conditions, and reference FM at  $\theta=14^\circ$ . The solidity,  $s$ , is the ratio of the total rotor blade area to the rotor disk area. A photo of the model is shown in Fig. 3 (airplane mode). The best hover data was obtained with the wind tunnel turned off and the rotor in airplane mode. This avoids ground effect on the rotor wake and figure of merit. Further details about the TRAM wind-tunnel test can be found in [5-6].

Rotor Radius, $R$	57 inches
Solidity, $s$	0.105
Tip Chord, $c_{tip}$	5.5 inches
Blade Twist	$32^\circ$ to $-6^\circ$ , nonlinear
Reynold's Number ( $c_{tip}$ ), $Re$	2.1 million
Tip Mach Number, $M_{tip}$	0.58, 0.62
Thrust Coefficient, $C_T/s$	0.05-0.17
Collective Pitch Angle, $\theta$	$3^\circ$ to $17^\circ$
FM Experimental Error	$\pm 0.005$
Reference FM at $\theta=14^\circ$	0.780

**Table 1** TRAM geometric characteristics and nominal hover test conditions.



**Figure 3** TRAM 1/4-scale model in airplane mode at the DNW wind tunnel.

## 3. Numerical Approach

The TRAM rotor blades are shorter and stiffer than a typical helicopter rotor. Their design is dictated by the need to function both as a propeller (airplane mode) and as a rotor (helicopter mode). The high inboard pitch angle and twist distribution along the blade span is more akin to a UAM rotor. The stiff rotor blades can therefore be treated as rigid and are ideally suited for assessing numerical aerodynamic accuracy without the complication of aeroelastic deflections.

The OVERFLOW CFD code is used to solve the time-dependent Navier-Stokes equations for the isolated TRAM rotor in hover. This CFD code has a variety of implicit and relaxation algorithms that utilize upwind and central spatial differencing. Both single and dual-time integration options are available.

Curvilinear and Cartesian overset grids are used to model complex geometries and the surrounding flow domain. A variety of zero-, one-, and two-equation turbulence models are available to close the Reynolds-averaged Navier-Stokes (RANS) equations. For more complex flows, transition trip lines and models, and detached eddy simulation (DES) are useful code options. A more complete description of the OVERFLOW CFD code and its user’s manual can be found in [13-14]. Some of the key choices used in the present computations are described below.

### 3.1 Overset Grids

OVERFLOW solves the Navier-Stokes equations on structured overset grids. The current time-accurate approach consists of an inertial coordinate system, where near-body (NB) grids (Fig. 4) rotate through a fixed Cartesian off-body (OB) grid system (Fig. 5). This is a common approach used with OVERFLOW. The rotating NB grids resolve the flow in the vicinity of the rotor/hub while the fixed Cartesian grids resolve the rotor wake and efficiently expand the computational domain to the far field through progressively coarser “brick” grids. Each brick grid is twice as coarse in each coordinate direction as its neighbor.

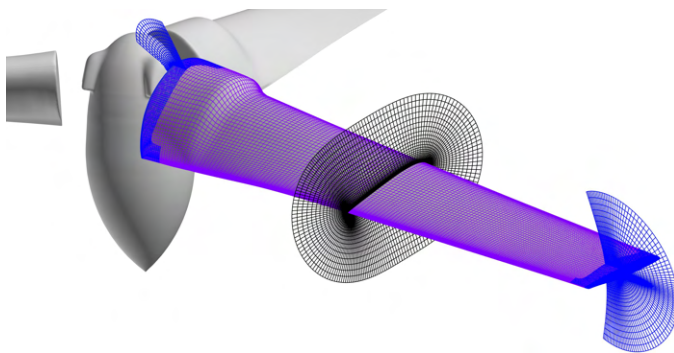


**Figure 4** TRAM NB curvilinear O-grids.

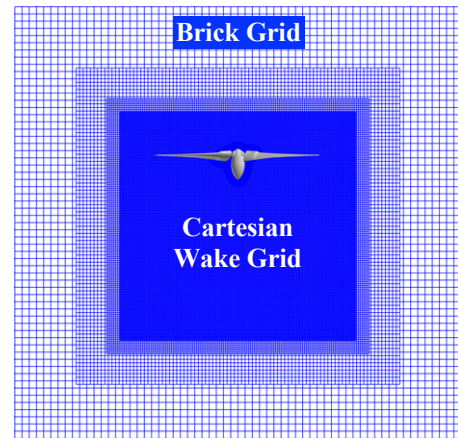


**Figure 5** TRAM rotor geometry imbedded in OB Cartesian grids.

Each rotor blade consists of a main O-mesh body grid and two O-mesh cap grids at the root and tip locations (see Fig. 4). The main rotor O-mesh consists of 181x175x66 grid points in the chordwise, radial, and body-normal directions. The surface-grid spacing in the chordwise ( $\Delta c$ ) and radial ( $\Delta r$ ) directions do not exceed 15% stretching ratio, while the body-normal grid spacing does not exceed 20% stretching ratio. The first three body-normal grid cells have uniform grid spacing to improve skin-friction and torque coefficient computations. The outermost boundary extends about 1 chord length from the blade surface with a grid spacing of  $\Delta = 5\%c_{tip}$ . A 20% stretching ratio should be viewed as the absolute maximum, and 15% is more desirable. The average y-plus one grid cell off the blade surface is  $y^+ \approx 0.2$ . Details of the surface grid spacing, and number of grid points are summarized in Tables 2-3. The O-mesh at the blade trailing edge (TE) provides adequate resolution of the confluent upper and lower boundary layers as they merge and diffuse downwind of the trailing edge, regardless of the blade’s collective angle or flow conditions. Usually 10-16 blunt TE grid cells are adequate to resolve and maintain the trailing-edge flow downwind of the blade.

$\Delta r_{ave}/c_{tip}$	$\Delta c_{ave}/c_{tip}$	$\Delta c_{LE}/c_{tip}$	$\Delta c_{TE}/c_{tip}$	No. TE Grid Cells
0.36%	1.56%	0.11%	0.03%	10

**Table 2** Average TRAM rotor-blade grid spacing near the outboard blade tip, including leading and trailing edge values.

Grid Type	Grid No.	Grid Points
Rotor Blades	1-9	11,355,696
Hub	10-12	1,915,518
Total NB Grids	1-12	13, 271,214

**Table 3** TRAM rotor-blade grid system.

### 3.2 Dynamic Adaptive Mesh Refinement

Buning and Pulliam [15] introduced an AMR process within OVERFLOW to dynamically resolve flow features with finer meshes using off-body Cartesian grids. An example of a multilevel OB-AMR process is shown in Fig. 6. The baseline Level-1 ( $L_1$ ) Cartesian grid is shown in light blue and surrounds the rotor with a grid spacing of  $\Delta S$ , often taken as  $10\%c_{tip}$ . The rotor wake can be further refined with AMR through successively finer overlapping Cartesian grids. Each level of refinement decreases the local grid spacing by a factor two in each coordinate direction, i.e., the refinement is isotropic in space. In this way a two-level OB-AMR refinement would overlay the surrounding  $L_1$  Cartesian grid with two finer Cartesian meshes, each with grid spacing  $\frac{1}{2}\Delta S$  and  $\frac{1}{4}\Delta S$ , respectively. The local grid size grows by 8 times with each level of refinement, and the portion of underlying meshes that are not used are “blanked out” in the code. Information is transferred between overset meshes using tri-linear interpolation. In this way the rotor wake can be refined to any desired level.

A somewhat different strategy is taken here that eliminates interpolation errors within the resolved rotor wake, see Fig. 7. This is accomplished by only using  $L_1$  grids to automatically capture and resolve the rotor wake where needed, i.e., no multi-level refinement. (One often knows a priori how much grid is computationally affordable and needed for FM accuracy.) These Level-1 Cartesian wake-grids share the same grid spacing,  $\Delta S_{wake}$ , and therefore have coincident grid points when they overlap with each other. Data is therefore transferred between these  $L_1$  wake grids by direct injection, i.e., no interpolation is required. Tri-linear interpolation is only

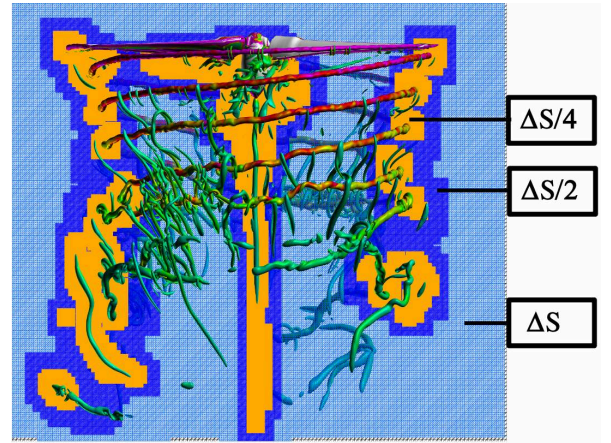


**Figure 6** Example of an OVERFLOW two-level AMR grid system for a rotor in hover.

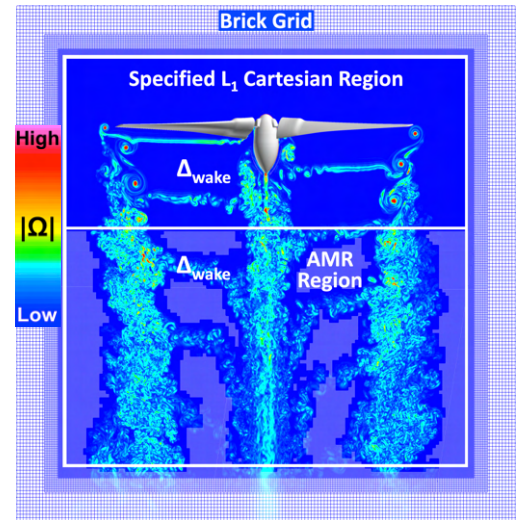


**Figure 7** Cutting plane and OB-AMR grids colored by vorticity magnitude for TRAM hover.

needed when dissimilar grids overlap with each other, see for example the coarser grids that overlap the  $L_1$ -grids in Fig. 7.

The strategy used in Fig. 7 (and throughout this paper) specifies a single Cartesian region just large enough to encapsulate the rotor/hub geometry. This Cartesian grid extends  $0.2R$  in the radial direction beyond the blade tip,  $0.35R$  above the rotor blades, and  $0.65R$  below the rotor blades. The lower AMR Region extends the wake-grid  $L_1$  resolution to  $2R$  below the rotor blades. Additional “brick grids” are added to these two regions to rapidly extend the computational domain to the far field, which for the present computations is  $17$  rotor radii ( $R$ ) from the blades. Yoon et al. [16] reported that the asymptotic limit of FM is achieved when the far-field boundary is at least  $15R$  from the rotor. The baseline (coarsest) grid system used in this paper has a wake-grid spacing  $\Delta_{\text{wake}}=10\%c_{\text{tip}}$ . This results in a total of  $39$  million grid points.

The AMR process depends on a sensor function ( $SF$ ) and user-specified parameters that automatically identify important flow gradients and determines where to refine, coarsen, or leave the grid resolution unchanged. Chaderjian et al. [4, 7] previously used a vorticity magnitude sensor function for OB-AMR. With this approach, once a threshold is reached, grid refinement is carried out to the fullest amount specified. A two-level refinement will refine the local mesh to  $\Delta S/4$  (Fig. 6), or a three-level refinement to  $\Delta S/8$ , etc.

Another option, and the one used in this paper, is based on  $Q$ , the solution vector of conserved variables (see Section 3.3). This  $SF$  is defined by the undivided difference

$$SF = \max_{i=j,k,l} \left\{ \max_{Q \text{ components}} \left[ \left( \frac{Q_{i-1} - 2Q_i + Q_{i+1}}{2 Q_{ref}} \right)^2 \right] \right\} \quad (2)$$

The term “undivided” refers to the difference not being divided by the appropriate grid cell size. Note that the  $SF$  has the following properties: (a) normalized by a reference quantity  $Q_{ref}$ , (b) squared to create a non-negative value, (c) takes the maximum value over all elements of  $Q$ , and (d) takes the maximum value over all coordinate directions. This function is non-dimensional, independent of grid units, and becomes smaller as the grid is refined (where  $Q$  is smooth), all desirable properties for a sensor function. Equation 2 therefore refines the local mesh in regions of high solution curvature. The AMR process is carried out in such a manner so that all adjacent overlapping grids differ by no more than 2 times the grid spacing, see Figs. 6-7. Further details of the OB-AMR process are described by Buning and Pulliam [15].

OVERFLOW can also carry out NB-AMR on the body grids, similar to the OB-AMR procedure. However, the NB-AMR operates on curvilinear grids, which look Cartesian in computational (or index) space. Parametric cubic interpolation is used to transfer data between NB grids of different resolution. This approach preserves smooth geometry, avoiding faceting of the body surface that would occur with tri-linear interpolation. Near-body AMR has some practical things to consider when refining body grids. The isotropic refinement tends to over resolve the boundary layer in the body-normal direction and may lead to a lack of solution robustness. Chaderjian [17] describes some strategies to circumvent these problems, but it is currently not recommended for routine applications. A non-isotropic formulation could greatly improve its computational efficiency and solution robustness. However, in its current implementation it can be used to establish solution grid convergence for non-periodic body grids. In the case where NB grids use periodic O-meshes, these grids must be split into overlapping non-periodic grids, see for example Chaderjian [17]. Further details of the NB-AMR process are described by Buning and Pulliam [18].

### 3.3 Solution Algorithm

The time-dependent Navier-Stokes equations can be written in strong conservation-law form and generalized curvilinear coordinates [19] as

$$\frac{\partial \widehat{Q}}{\partial t} + \frac{\partial(\widehat{F}-\widehat{F}_v)}{\partial \xi} + \frac{\partial(\widehat{G}-\widehat{G}_v)}{\partial \eta} + \frac{\partial(\widehat{H}-\widehat{H}_v)}{\partial \zeta} = \mathbf{0} \quad (3)$$

where  $Q = [\rho, \rho u, \rho v, \rho w, e]^T$  is the vector of conserved variables,  $\rho$  the density,  $u, v$ , and  $w$  the Cartesian velocity components, and  $e$  the total energy per unit volume. Also,  $\widehat{Q} = Q/J$  is the transformed variables,  $J$  the coordinate transformation Jacobian,  $\widehat{F}$ ,  $\widehat{G}$ , and  $\widehat{H}$  are the transformed inviscid flux vectors, and  $\widehat{F}_v$ ,  $\widehat{G}_v$ , and  $\widehat{H}_v$  are the transformed viscous flux vectors.

One approach to solving this time-accurate problem is to introduce a second artificial ‘‘dual-time’’ term according to

$$\frac{\partial \widehat{Q}}{\partial \tau} = - \left[ \frac{\partial \widehat{Q}}{\partial t} + \frac{\partial(\widehat{F}-\widehat{F}_v)}{\partial \xi} + \frac{\partial(\widehat{G}-\widehat{G}_v)}{\partial \eta} + \frac{\partial(\widehat{H}-\widehat{H}_v)}{\partial \zeta} \right] \quad (4)$$

Here the goal is to drive the pseudo time integration of the fixed point to zero ( $\partial \widehat{Q} / \partial \tau = \mathbf{0}$ ), i.e., steady-state in  $\tau$ . This approach allows for the use of steady-state methods to efficiently solve time-dependent problems through a subiteration process in  $\tau$ . The converged result satisfies Eq. 3 at the completion of each time step.

Chaderjian et al. [4, 7] previously solved Eq. (3) for the TRAM in hover using the Pulliam-Chaussee diagonal algorithm [20] within the context of a dual-time formulation, i.e., Eq. (4). The key advantage to using this central-difference method is its computational efficiency, i.e., its diagonal form and use of scalar implicit solvers. One of the drawbacks to this central scheme was its lack of robustness in simulating more challenging forward-flight problems, like dynamic stall [17].

A different dual-time approach is used in the current OVERFLOW TRAM simulations, i.e., the HLLE++ upwind algorithm [21] together with an unfactored symmetric successive over relaxation (SSOR) [22] solver, that does not exhibit the robustness issues encountered in [17]. The HLLE++ algorithm also has the following desirable properties:

Captures stationary grid-aligned shocks over $\approx 2$ grid points
No expansion shocks (no entropy fix required)
<b>Reduced dissipation for boundary layers</b>
Exact capture of stationary contact discontinuities
Much reduced susceptibility to carbuncles

**Table 4** Properties of the HLLE++ upwind algorithm [21].

where the third property is the most relevant of the five for the present application. It will be later shown that this leads to more physically correct vortex core sizes. The dual-time process also updates the zonal boundary data at the completion of each subiteration step. In this way the zonal overset boundaries converge to the new time level. SSOR is currently implemented in OVERFLOW with 10 backward and forward sweeps for each dual-time subiteration step.

The use of an SSOR solver has facilitated several recent improvements into the OVERFLOW code, i.e., implicit physical boundary conditions and improved linearization of the implicit operator [13]. These improvements together result in greater solution robustness and improved solution convergence than applications solved with the original central scheme [4, 7, 17, 20]. The HLLE++/SSOR algorithm is about three times more expensive per subiteration than the central scheme. However, its ability to achieve solution convergence with fewer subiterations makes it computationally competitive with the central scheme, especially for problems with difficult flow physics.

The dual-time step procedure was optimized on a representative baseline case to reduce computational cost. A constant Courant-Friedrichs-Lewy (CFL) condition provides an excellent way to drive the dual-time subiteration process to rapid convergence with the SSOR approach. Figure 8a shows how the  $L_2$ -norm of the Navier-Stokes residual varies with CFL number. Note that the best convergence occurs near CFL=75. At this optimal condition, Fig. 8b shows how the residual drops with dual-time subiterations. A

value of 16 subiterations was used throughout this paper and maintained at least a 2-order drop for all cases and grids. Note that the HLLE++/SSOR algorithm remains stable at a large CFL condition, see Fig. 8a.

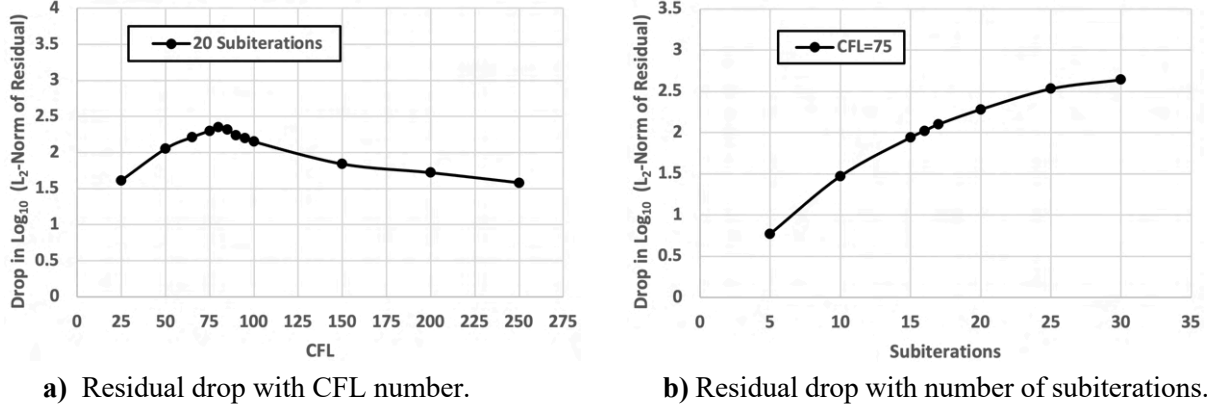


**Figure 8** Baseline convergence optimization.

### 3.4 Turbulence Model

All of the rotor simulations in this paper use the one-equation Spalart-Allmaras (SA) [23] turbulence model. Computed results will show that the details of the SA turbulence model play an important role in the accurate prediction of FM. Some of the model’s key features are now described.

The SA model uses the Boussinesq approximation to relate the Reynolds stresses to a kinematic turbulent eddy viscosity and the mean strain-rate tensor. The turbulent eddy viscosity (TEV) is given by

$$\nu_t = \tilde{\nu} f_{\nu 1}$$

The SA transport equation for the variable  $\tilde{\nu}$ , is given by

$$\frac{D\tilde{\nu}}{Dt} = \underbrace{C_{bl}\tilde{\nu}\left(\Omega + \frac{\tilde{\nu}}{k^2 d^2} f_{\nu 2}\right)}_{\text{Production}} - \underbrace{C_{wl}f_w\left(\frac{\tilde{\nu}}{d}\right)^2}_{\text{Destruction}} + \underbrace{\frac{1}{\sigma}\left[\nabla \cdot \left((\nu + \tilde{\nu})\nabla\tilde{\nu}\right) + C_{b2}(\nabla\tilde{\nu})^2\right]}_{\text{Diffusion}} \quad (5)$$

where  $D/Dt$  is the material time derivative. The right-hand side consists of production, destruction, and diffusion source terms. The constants  $C_{bl}$ ,  $C_{b2}$ ,  $C_{w1}$ ,  $k$ ,  $\sigma$ , and functions  $f_{\nu 1}$ ,  $f_{\nu 2}$ ,  $f_w$ , are described by Spalart and Allmaras [23], and  $\Omega$  is the magnitude of vorticity. The damping function,  $f_{\nu 1}$ , reduces  $\nu_t$  near a solid wall, i.e., the laminar sublayer. The turbulent length scale,  $d$ , is defined as the distance between a field point and the nearest wall.

Rotor blade vortices are a dominant structure in the turbulent rotor wake. They are initially formed at the rotor tip by the roll-up of the blade trailing edge shear layer. Figure 9 is a laser light sheet flow visualization of a fully formed tip vortex reported by Ramasamy et al. [24]. The rotor trailing-edge shear layer contains the blade’s bound vorticity that is initially formed on the upper and lower surfaces of the rotor blades. These shear layers are stretched and elongated in the rotor wake as they are entrained into the vortex. This vortex stretching process can be thought of as a tube of vorticity whose diameter decreases as it elongates, resulting in higher levels of vorticity and turbulence, while conserving circulation. Ramasamy et al. [24] identified three regions of a developed vortex, see Fig. 9. According to Ramasamy, the outer region 3 can be characterized by a turbulent flow whose mean velocity field is similar to a potential vortex. Region 2 is an intermediate state that contains turbulent eddies of varying size. The inner-most region 1 can be characterized as stratified layers having few or small eddies with little interaction between fluid layers, due to high streamwise curvature. This inner-core region has a near-linear velocity profile and very low fluid strain. Gray [25-26] experimentally observed that the trailing edge vortex sheet (shear layer) descends downward at a faster rate than the tip-vortex helix, see Fig. 10. This is due to an induced downwash by the thrust-producing rotor blades.

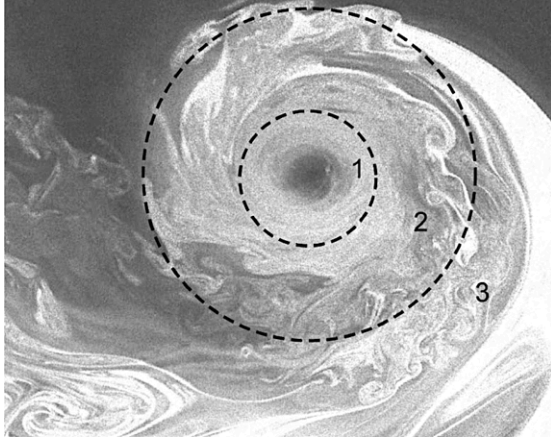


**Figure 9** Laser light sheet flow visualization of a fully developed blade-tip vortex, Ramasamy et al. [24].

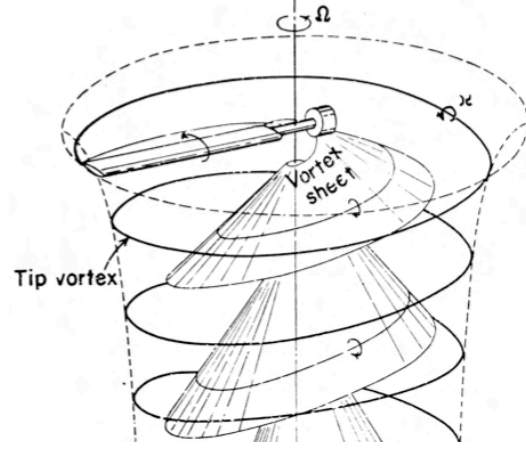


**Figure 10** Sketch by Gray [25-26] of an observed descending wake shear layer.

Shur et al. [27] introduced a SA rotation and/or streamline curvature (SARC) correction for rotating and curved flows. The SARC correction not only improves the boundary layer profiles for highly curved flows, but also helps reduce the TEV in the tip vortex cores. This correction models the reduced mixing and very low strain in region 1 of Fig. 9. The SARC correction is used for all SA turbulent simulations in this paper.

An additional degree of realism can be obtained by the use of large eddy simulation. In LES the largest turbulent eddies within a boundary layer are resolved using an appropriate small grid spacing,  $\Delta$ , and the subgrid-scale (SGS) eddies are modeled. Smagorinsky [28] first postulated a SGS model for the Reynold's stresses based on the following expressions

$$\tau_{ij} = 2\nu_t S_{ij}, \quad S_{ij} = \frac{1}{2} \left( \frac{\partial u_i}{\partial x_j} + \frac{\partial u_j}{\partial x_i} \right) \quad (6)$$

where  $S_{ij}$  is the resolved strain-rate tensor,  $\nu_t$  is the Smagorinsky eddy viscosity given by

$$\nu_t = (C_s \Delta)^2 \sqrt{S_{ij} S_{ij}} \quad (7)$$

and  $C_s$  is the Smagorinsky coefficient. In this expression,  $\Delta = (\Delta x \Delta y \Delta z)^{1/3}$ , i.e., the geometric mean of the grid cell spacing. Use of wall-resolved LES throughout the entire flow domain is beyond current computational capability for rotor flows at typical flight Reynolds numbers. This is due to the disparate length scales of wall-bounded flows, e.g., the boundary layer on a rotor blade. However, Spalart et al. [29] suggested detached eddy simulation (DES) as a more practical alternative.

DES can be viewed as a blending of a RANS turbulence model within the boundary layer and coarse-mesh LES outside the boundary layer. It was originally developed to treat separated flow where the largest eddies can be grid resolved. However, this hybrid RAN/LES turbulence model can also resolve the largest turbulent scales due to the interaction between a rotor's shear layers and tip vortices. This is accomplished in the SA turbulence model (Eq. 5) by replacing the distance from a field point to the nearest surface ( $d$ ) by

$$\bar{d} = \min(d, C_{DES} \Delta) \quad (8)$$

where  $C_{DES} = 0.65$  and  $\Delta = \max(\Delta x, \Delta y, \Delta z)$  is the maximum local grid spacing. Note that  $\Delta$  is characterized by the grid spacing along a blade surface and not normal to it. In this way the SA-RANS model becomes the SGS model for turbulent scales within the boundary layer, assuming  $\Delta$  is larger than the boundary layer thickness. Moreover, it is easy to show that when production balances destruction in Eq. 5, and when  $\bar{d}$  is used as the length scale, then  $\nu_t$  simplifies to a Smagorinsky-type model. So the SA-DES model behaves like an LES-type model, modeling turbulent scales within the boundary layer (using RANS as the SGS model) and grid-resolving the largest turbulent scales outside the boundary layer.

However, there is potential danger in using DES in conjunction with excessive grid refinement along a solid wall, e.g., too much NB-AMR. The intent of DES is to be in RANS mode throughout the boundary layer and LES mode outside the boundary layer, where the largest turbulent scales can be grid-resolved. As previously mentioned, proper use of DES involves the wall-parallel spacing being greater than the boundary layer thickness,  $\Delta l > \delta$ . If the wall-parallel grid spacing is much smaller than the boundary layer thickness, then LES-mode can be prematurely activated and the Reynolds stress will be artificially too small. This modeled stress depletion (MSD) can cause premature separation and give non-physical results.

This situation can be avoided by making sure the grid spacing parallel to the wall is larger than the attached boundary layer thickness. However, Spalart et al. [30] also introduced a correction called delayed detached eddy simulation (DDES). This algebraic formula helps prevent the inadvertent use of LES mode within a boundary layer, ensuring the RANS model is active throughout the boundary layer. This correction works very well most of the time, but it can fail. None of the grid spacings in this study are fine enough to inadvertently activate LES mode within the boundary layer. Therefore, only the DES option has been used. The use of DDES is perhaps a prudent precaution to use in general, however, it would not change any of the results reported in this paper.

## 4. Results and Discussion

The OVERFLOW CFD code is used to solve the time-dependent Navier-Stokes equations for an isolated V22 (TRAM) rotor in hover and fully turbulent flow, where the tip-chord Reynolds number is  $Re=2.1$  million. No effort is made to model turbulent flow transition and solutions are free from the influence of the ground or vehicle components, e.g., fuselage. The viscous Navier-Stokes equations are applied throughout the entire computational domain using 2<sup>nd</sup>-order time accuracy with a physical time step of  $\Delta t=1/4^\circ$  of rotation. This time step is a typical choice by many and has been shown to be sufficient to temporally resolve the relevant flow features both for hover and forward flight [10, 31, 32]. Chaderjian [17] describes a method to quantify the temporal convergence of the CFD forces and moments by comparing RMS waveforms with the change of numerical parameters.

The objective in the following sections is to examine how numerical choices affect the accurate prediction of FM. Moreover, the use of OB-AMR and time-dependent flow visualization is used to explore the numerical and physical nature of the rotor wake.

### 4.1 Spatial Accuracy

The baseline flow condition described in this section has a collective pitch angle of  $\theta=14^\circ$ , blade tip Mach number  $M_{tip}=0.625$ , and the Reynolds number based on tip chord  $Re=2.1$  million. This corresponds to a high-thrust wind-tunnel case [5-6], where the measured figure of merit is  $FM_{EXP}=0.780\pm 0.005$ . Appropriately sized fine body meshes, especially at the outboard blade tip, are summarized in Tables 2-3. Figure 11 shows a 5<sup>th</sup>-order upwind result with a baseline OB-AMR rotor-wake resolution of  $\Delta_{wake}=10\%c_{tip}$ , where the grids are colored by vorticity magnitude. At this resolution, the entire OB-AMR region is filled with a uniform  $\Delta_{wake}$  grid spacing. Weak vortex pairing begins to form near the lower boundary of the specified  $L_1$  region, while vortex breakdown occurs in the OB-AMR region. Vortex pairing and eventual breakdown occur because of the strong tip vortices associated with high thrust

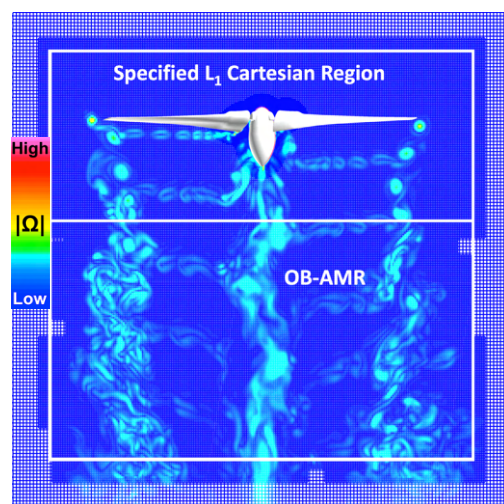


**Figure 11** Baseline OB-AMR grids colored by vorticity magnitude,  $\Delta_{wake}=10\%c_{tip}$ .

and high blade twist along this propeller-like rotor. Recall that there is no inter-grid interpolation between these tightly converged  $L_1$  grids. The total grid system has 39 million grid points.

Figure 12 shows the rotor wake system (iso-surfaces of the  $q$ -criterion), a cutting plane colored by vorticity magnitude, and FM using different HLLC++ spatial accuracies with the SA-RANS turbulence model. Note that the 3<sup>rd</sup>-order accurate vortex wake dissipates quickly at an early wake age (Fig. 12a). Moreover, the 3<sup>rd</sup>-order option underpredicts the experiment FM by 2.4%. Indeed, this result reflects both the approach and accuracy reported in the 2009 state-of-the-art assessment [1]. On the other hand, 5<sup>th</sup>-order spatial accuracy preserves the vortex wake to a much larger wake age and includes weak vortex pairing and vortex breakdown, see Fig. 12b. Moreover, the FM difference between CFD and experiment is now reduced to 1.1%. This improvement reduced the discrepancy by more than 50%, and is getting close to the goal of  $\Delta FM = \pm 0.005$  of the experiment. Figure 12c shows the vortex wake using 3<sup>rd</sup>-order spatial differences on the NB-grids and 5<sup>th</sup>-order spatial differences on the OB-grids. The vortex wake looks similar to that of Fig. 12b, however, the FM is in between the pure 3<sup>rd</sup>- and 5<sup>th</sup>-order results. This shows higher-order spatial accuracy does improve the prediction of FM by better resolving the flow on the blades (bound vorticity), and it preserves the tip vortices to a greater wake age.

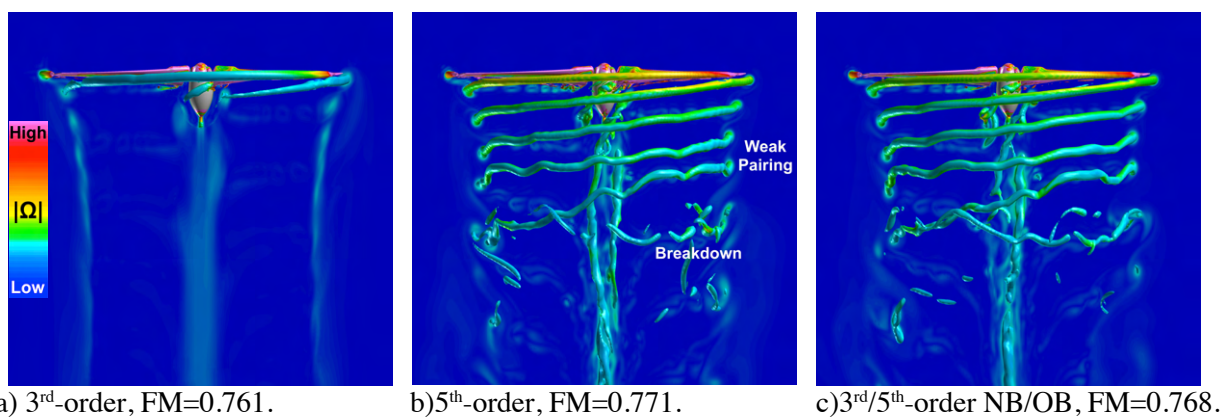


**Figure 12** Effect of spatial accuracy on FM, rotor vortices, and cutting plane of vorticity magnitude. SA-RANS,  $\theta=14^\circ$ .

## 4.2 Turbulence Models

The previous section demonstrated the importance of using high-order spatial accuracy together with the grid spacing shown in Tables 2-3. The 5<sup>th</sup>-order FM showed more than a two-fold improvement in agreement with experiment over the 3<sup>rd</sup>-order FM. Attention is now given to how the turbulence model effects the prediction of FM.

Figure 13 shows the vortex wake and a cutting plane colored by vorticity magnitude using the SA-DES turbulence model, 5<sup>th</sup>-order upwind differencing, and  $\Delta_{wake}=10\%c_{tip}$ . The reduced TEV, due to the reduced DES length scale, allows for a much richer and detailed turbulent wake. Instabilities such as vortex pairing and vortex breakdown are much easier to identify. The SA-RANS turbulence model diffuses and dissipates these phenomena (compare with Fig. 12b). Figure 13 also

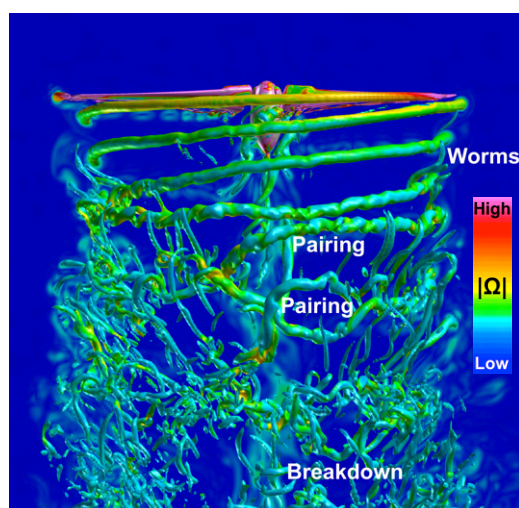


**Figure 13** Effect of 5<sup>th</sup>-order spatial accuracy on vortex wake and cutting plane colored by vorticity magnitude. FM=0.776, SA-DES,  $\theta=14^\circ$ .

identifies a phenomenon Chaderjian et al. [4, 7] first called “turbulent worms”, while others [31] later referred to these as secondary vortices. These worms did not appear using  $\Delta_{\text{wake}}=10\%c_{\text{tip}}$  with central differences [4, 7], but required a finer resolution of  $\Delta_{\text{wake}}=5\%c_{\text{tip}}$ . This further illustrates that the HLLC++ upwind algorithm has less dissipation than the original central scheme.

The lower TEV also improves the predicted figure of merit, i.e.,  $\text{FM}=0.776$ . This value now underpredicts the experiment by only 0.5%. This reduces the prediction error from the 2009 assessment [1] by 5 times. Doubling the grid resolution on the rotor blades in each coordinate direction only changes the FM to 0.778. This is a very small change, indicating that the baseline body-grid spacings in Tables 2-3 are grid-converged with respect to FM. Table 5 summarizes the prediction accuracy of FM using various combinations of spatial accuracy and turbulence models. Both are important at this high thrust setting.

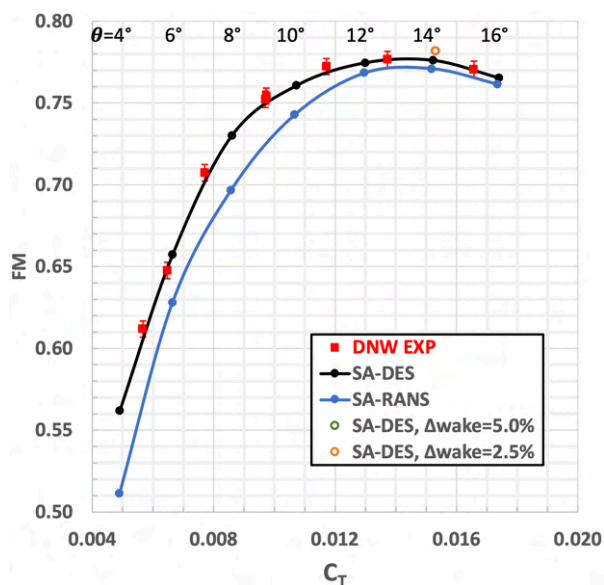
Spatial Diff	$\text{FM}_{\text{RANS}}$	$\Delta\text{FM}_{\text{EXP}}$	$\text{FM}_{\text{DES}}$	$\Delta\text{FM}_{\text{EXP}}$
3 <sup>rd</sup> -Order	0.761	-2.40%	0.767	-1.70%
5 <sup>th</sup> -Order	0.771	-1.16%	0.776	-0.50%

**Table 5** Summary of predicted FM using different spatial accuracy and turbulence models. Baseline NB grids (Tables 2-3) and  $\Delta_{\text{wake}}=10\%c_{\text{tip}}$ .

The FM computed for a collective sweep using 5<sup>th</sup>-order upwind differences together with the SA-RANS and SA-DES turbulence models are compared with experiment in Fig. 14, where  $\Delta_{\text{wake}}=10\%c_{\text{tip}}$ . The turbulence models are active throughout the entire computational domain. The SA-DES turbulence model accurately predicts the FM within experimental error for all displayed collectives and thrust coefficients. (Chaderjian and Buning [4] first obtained this result in 2011 using central differencing.) On the other hand, the SA-RANS turbulence model somewhat underpredicts the FM for the higher collectives and significantly underpredicts the FM for the lower collectives, beginning near  $\theta=10^\circ$ .

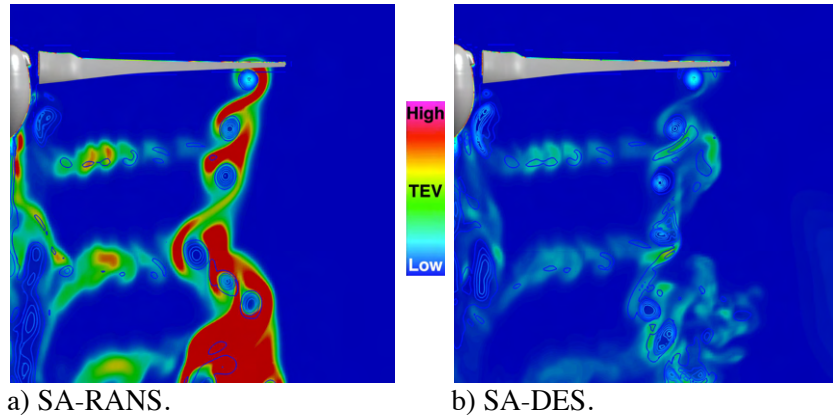
The problem with the RANS model is the length scale “d.” Deep within the rotor wake, say one or two blade radii below the rotor blades, the large value of “d” forces the turbulent destruction term in Eq. 5 towards zero. This allows undamped growth of turbulent production and TEV near high vorticity regions, i.e., the tip vortices. On the other hand, the DES length scale,  $\bar{d}$ , is much smaller and allows the destruction term in Eq. 5 to remain active. This provides a counterbalance to the turbulent production, resulting in smaller TEV values. It is also a more realistic measure of the larger resolvable turbulent scales in the rotor wake. The local grid spacing functions as an implicit filter for the smaller unresolved turbulent scales, which are accounted for with reduced DES TEV. Detached eddy simulation is a simple, elegant, and practical approach to modeling the turbulent flow in a rotor wake.

Figure 15 shows a cutting plane colored by TEV for  $\theta=14^\circ$ . The high TEV is evident in the high-vorticity region of the entrained wake shear layers, see Fig. 15a. This is caused by high local vorticity and



**Figure 14** CFD prediction of FM for the 1/4-scale TRAM model.

the large RANS length scale, as previously discussed. Notice also that the SARC curvature correction does maintain lower TEV in the vortex cores, but this is not enough to keep the TEV low elsewhere. The high TEV extends upward enough to interact with the rotor blades, causing a local increase in shear stress (drag) and drag moment (torque). This artificially lowers the RANS FM by a small amount. On the other hand, the DES TEV is much lower throughout the entire rotor wake and blade regions, see Fig. 15b. Here the turbulent production and destruction are in better balance with each other and do not interfere with the rotor performance.



**Figure 15** Cutting plane colored by TEV,  $\theta=14^\circ$ .

Figure 16 provides a similar comparison of TEV for  $\theta=8^\circ$ , a collective that significantly underpredicts the experiment's FM with the RANS turbulent length scale (see Fig. 14). Notice the high RANS TEV not only penetrates the interior of the rotor wake, but also outside the vortex sheet and above the rotor blades. This significantly reduces the FM due to the blades increased drag and torque. Fig. 16b again demonstrates a lower DES TEV throughout the entire rotor wake and blade regions, and does not interfere with the rotor performance (see Fig. 14).

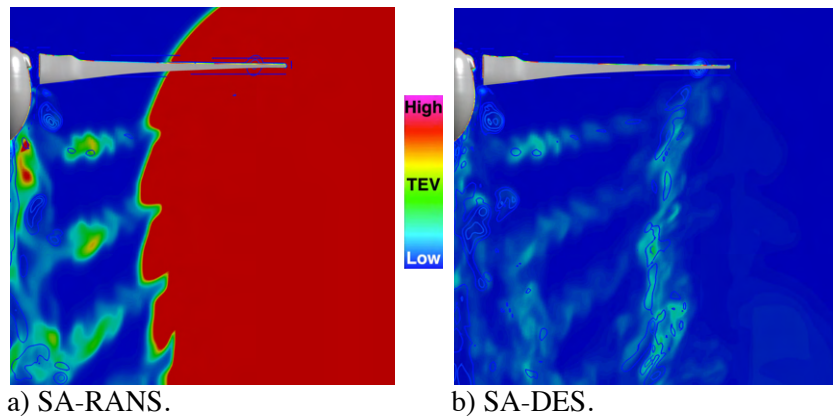


**Figure 16** Cutting plane colored by TEV,  $\theta=8^\circ$ .

The development and progression of high RANS TEV with time is shown in Fig. 17 for  $\theta=8^\circ$ . One revolution from impulsive start, high TEV forms in the lower wake along the high-vorticity vortex sheet (shown with a dotted white line). At 3 revs, it has spread in width to the outboard side of the vortex sheet, including a larger region in the lower wake. It has also progressed upward near the rotor blades. At 10 revs, it dominates the outboard region of the vortex sheet. Moreover, the top tip-vortex entrains the high TEV inboard of the vortex sheet. This process is also apparent from the other vortices in the lower part of the vortex sheet. Finally at 50 revs, turbulent diffusion spreads the high TEV further into the central core

of the vortex wake, greatly reducing the RANS FM. This process illustrates that turbulent production, destruction, and diffusion each play an important role in the accurate prediction of FM and preserving wake details to a greater wake age. Moreover, the progression of RANS TEV throughout the vortex wake is a very slow process. It will be shown in the next section that this greatly slows down the convergence of RANS FM.

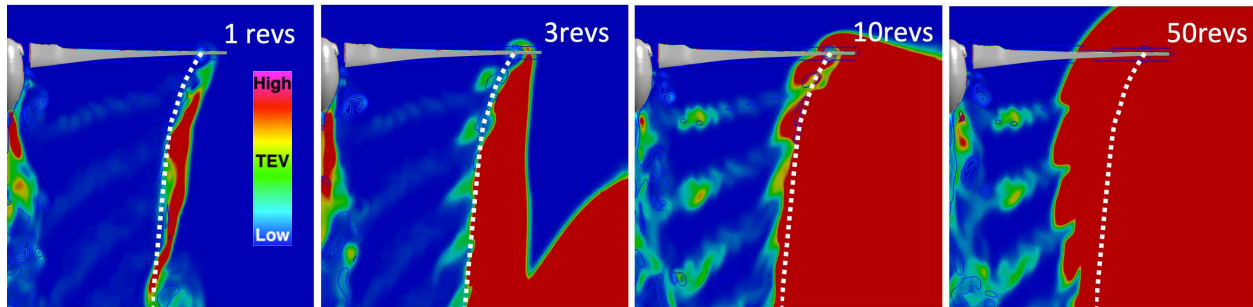


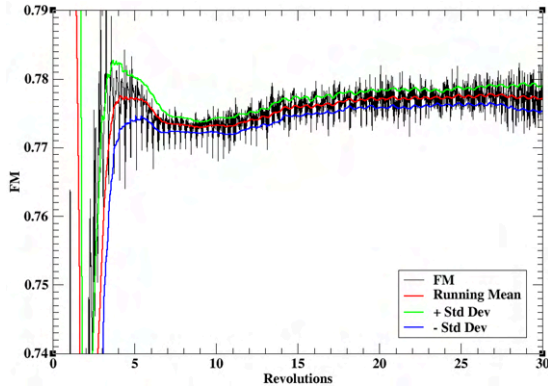
**Figure 17** Progression of SA-RANS TEV with time from impulsive start,  $\theta=8^\circ$ . Vortex sheet shown with white dots.

### 4.3 FM Convergence

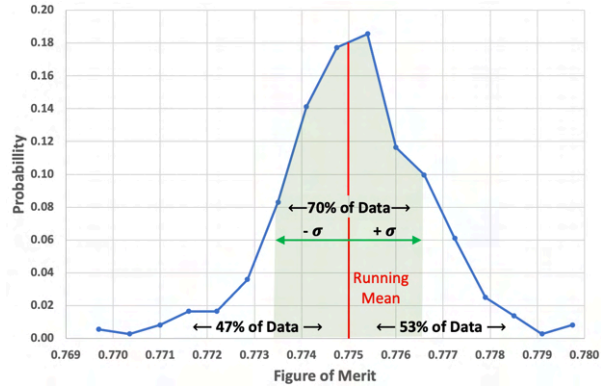
The FM is computed from the thrust and torque coefficients according to Eq. 1. However, the approach often taken is to average the CFD  $C_T$  and  $C_Q$  coefficients individually over several rotor revolutions and then evaluate the FM. This is consistent with the approach often taken in experiment, where the averaging is taken over many tens of revolutions. On the other hand, a CFD simulation may only be carried out over 10 or fewer revolutions from impulsive start, where much of the FM time-history is transitory and unusable to compute averages. Moreover, this simple averaging approach provides no additional information on solution convergence or how widely the FM varies over a rotor revolution. A statistical approach is taken here that quantifies the FM, its variance, and provides a means to specify when a solution is considered converged.

Figure 18 illustrates a typical FM response to an impulsive-start CFD solution. The periodic rotation of the rotor blades should ideally lead to a periodic response that eventually converges to a flat FM which is independent of the azimuth angle ( $\psi$ ). However, this is not the case during actual flight or even in a controlled experiment. For example, vortex pairing and chaotic fluctuations in the turbulent wake beneath the rotor blades can perturb the flow on the rotor blades, including the FM. The black curve in Fig. 18a corresponds to the instantaneous response of the TRAM FM to an impulsive-start CFD hover simulation, where  $\theta=14^\circ$ . There is a significant and rapid variation of the FM as the rotor sheds its starting vortex ring. As the solution develops and large-scale transients damp, the FM settles into what appears as a quasi-steady mean with a low amplitude, high-frequency oscillation. One natural way to filter the high-frequency components is to time-average the FM as a running mean based on the fundamental frequency of the rotor, i.e., one revolution. This is shown by the red curve. The software that computes the running mean also computes the standard deviation ( $\sigma$ ) of the data, which is also shown in Fig. 18a as green and blue curves. These provide a measure of the spread of the FM data.

As the solution evolves in time, the FM's running mean eventually reaches a converged value. The difference between the converged running mean and the FM computed by first averaging  $C_T$  and  $C_Q$  individually typically differs only in the 5<sup>th</sup> digit. A small standard deviation is the reason these two mathematically different approaches are in such close agreement. The FM running mean is therefore a reliable way to validate CFD solutions with experiment and used throughout this paper.



a) Time accurate FM from impulsive start.



b) PDF of FM.

**Figure 18** Convergence history of FM. TRAM rotor in hover,  $\theta=14^\circ$ , SA-DES.

The standard deviation also provides a measure of how much data is “near” the running mean. If the statistics follow a true gaussian, then 68.2% of the data fall within a band of one standard deviation. Figure 18b shows the probability distribution function (PDF) for the TRAM hover simulation. It looks very similar to a gaussian, and 70% of the data fall within a one  $\sigma$  band. The standard deviation can therefore be used to quantify how many significant digits are meaningful in the running mean FM. If  $\sigma$  is on the order of the 3<sup>rd</sup> digit, then three digits are meaningful to report. If it is on the order of the 2<sup>nd</sup> digit, then two digits are meaningful to report. Recall that  $\Delta FM=0.005$  is equivalent to the weight of one passenger. It is therefore desirable to report the 3<sup>rd</sup> digit when statistically justified.

It is clear from Fig. 18a that it can take a long time for the FM to fully converge. Following the TRAM rotor shedding its start-up vortex ring, vortex pairing begins somewhere between 7-8 revolutions. It can take another 10 or more revolutions for the influence of the vortex pairing on the rotor blades to reach equilibrium, including the influence of the far-field boundaries and chaotic turbulent wake. Overall, it can take 20-30 revolutions to establish a meaningful 3-digit FM, depending on the collective. It may take even longer inside a wind-tunnel facility [33]. A quick-start procedure is needed to reduce computational costs to a more practical level.

Progress has been made to improve solution convergence and reduce computational cost by initializing the flow field and applying far-field boundary conditions with asymptotic solutions to the hover problem. This helps reduce the time needed for a low-speed flow to develop and reach the distant computational boundaries. Early attempts applied a source/sink asymptotic solution to the far-field boundaries [34]. This approach viewed the hover problem as an inviscid momentum source, where flow is drawn in from above (sink) and the rotor disk generates a quasi-one-dimensional flow (source) that is confined within a contracting stream tube that eventually reaches a constant diameter. The far-field boundary below the rotor is therefore a combination of inward flow from the sink and outward flow through a hole with diameter of the far-field stream tube. Characteristic boundary conditions are used to impose these far-field velocities. A different approach was demonstrated by Repsher and Spalart [35]. They viewed the far-field wake as eventually evolving into a self-similar turbulent jet. They also used characteristic boundary conditions to impose the asymptotic velocities onto the far-field boundaries. Spalart describes the theoretical basis for this model [36]. These asymptotic methods do improve solution convergence; however, they only apply to hover when there are no nearby physical boundaries. These asymptotic boundary conditions can’t be applied to problems where the outer boundary is too close to the rotor blades, e.g., a rotor in a test facility or a UAM in ground effect.

A numerical rather than theoretical approach is taken here that is general for any hover problem, even one with nearby solid boundaries, see for example Chaderjian and Ahmad [33]. A large class of numerical methods, including the one used here, utilize subiterations and a time step ( $\Delta t$ ) to converge the time-dependent solution to the next time level. Second-order time accuracy is established in the current TRAM hover simulations using the HLLE++ upwind algorithm with 16 subiterations, a physical time step of  $\frac{1}{4}$  degree of blade rotation, and CFL=75. This insures there is at least a 2-order drop in the  $L_2$ -norm subiteration residual for all grids. Each rotor revolution has 1,440 steps. However, the quick-start procedure reduces the CFL to 30 for start-up stability, the subiterations to 8, and increases the physical time step to  $\Delta t=2^\circ$  over the first 4,320 steps ( $3 \times 1,440$ ). This reduces the computational work by 16 times for each time step. The result is shown in Fig. 19. The first “three revolutions” ( $3 \times 1,440$  steps) really correspond to 24 physical blade revolutions. This allows the start-up transients to efficiently damp out and establish the rotor flow. Notice that the FM quickly transitions from this quasi-time-accurate flow to a time accurate flow (in the 2<sup>nd</sup>-order sense) within two rotor revolutions (revs 3-5). The running mean FM is relatively flat at 5 revolutions of work. The specific CFL, number of subiterations, and large time step used in the quick-start procedure will be problem dependent, i.e., flow conditions and geometry complexity. Numerical experiments have shown that the quick-start must be quasi time accurate. A safe choice is a 1-order drop in the subiteration residual. If the quick-start is too aggressive, e.g., 0-order drop, the solution may not fully recover the proper FM. All of the FM solutions presented in this paper use this quick-start procedure.

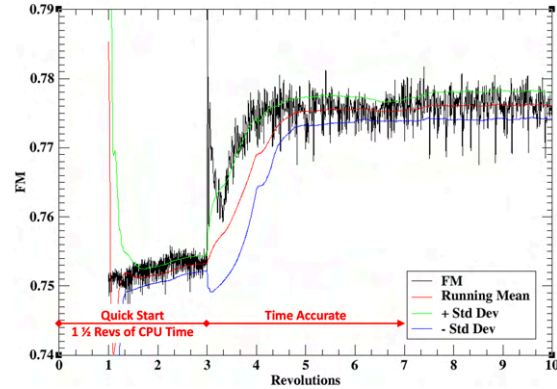


**Figure 19** Quick-start procedure, SA-DES,  $\theta=14^\circ$ .

Figure 20 illustrates the SA-DES and SA-RANS quick-start convergence for a  $10^\circ$  collective. The  $10^\circ$  DES case converges just as rapidly as the  $14^\circ$  DES case (compare with Fig. 19). In fact, all DES collectives showed a similar rate of convergence. However, the quick-start procedure did not work very well for the RANS cases, see for example Fig. 20b. The slow progression of large TEV onto the rotor blades and into the rotor wake, similar to that shown in Fig. 17, greatly slows down the convergence of the RANS FM, even with the quick-start procedure.

Figure 21 shows there is significant blade vortex interaction (BVI) at the lower collectives. This is responsible for the small “chatter” in DES FM as the solution takes time for the vortex position to settle down relative to the blade leading edge. Moreover, the “collision” of the vortex with a blade leading edge further spreads the large TEV over the rotor blade. Therefore, the SA-DES turbulence model is highly recommended over the SA-RANS turbulence model for hover simulations because: 1) its improved prediction accuracy of FM, 2) superior solution convergence, and 3) reduced computational cost using the quick-start procedure. Moreover, the SA-DES running mean FM had a typical standard deviation  $\sigma \approx \pm 0.002$  for all collectives, indicating the 3<sup>rd</sup> digit was meaningful and reported.

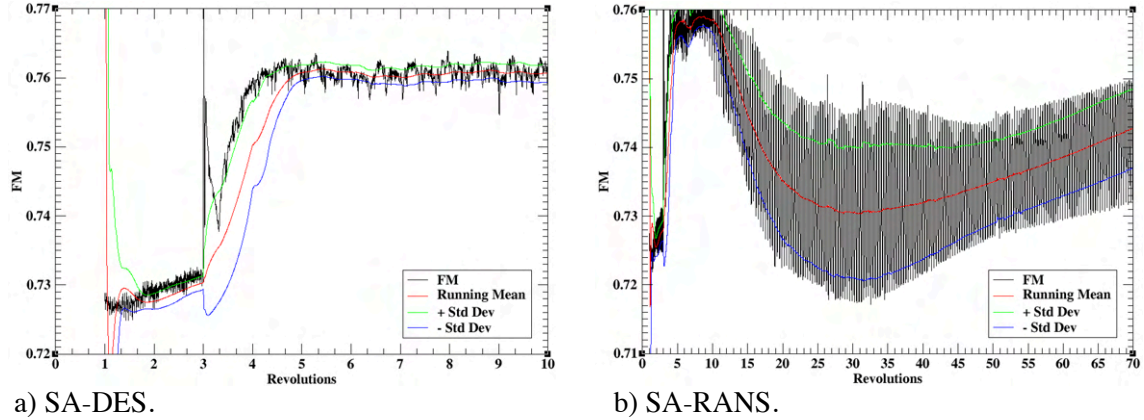


Figure 20 Quick-start convergence history of FM,  $\theta=10^\circ$ .

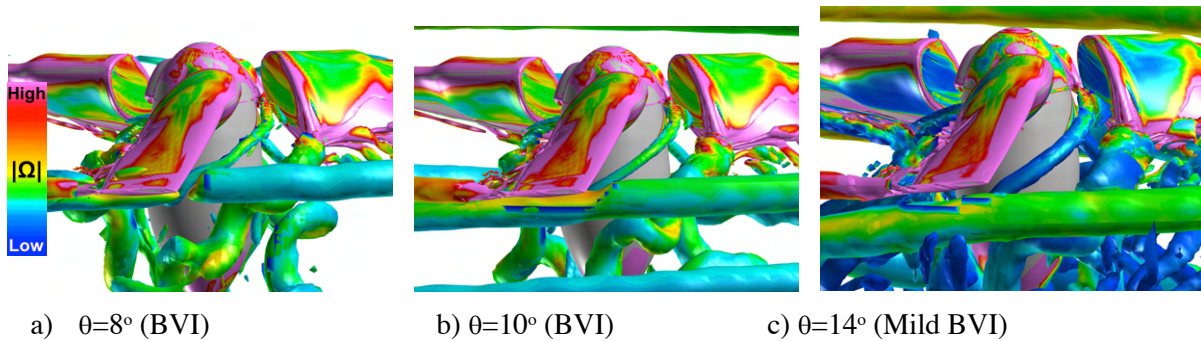


Figure 21 Blade vortex interaction at different collectives.

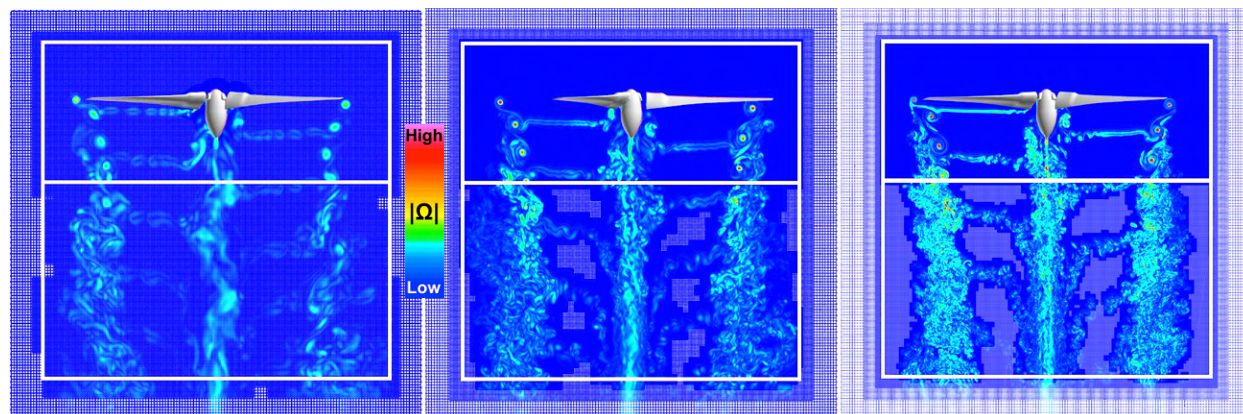
The above statistical approach also provides a rational framework to decide when the FM is sufficiently converged. The degree of convergence depends, of course, on the requirements for the simulation. The stopping criterion adopted here is for the running mean FM to remain bounded by  $\Delta FM = \pm 0.0005$  for two rotor revolutions to justify three-digit reporting, or  $\Delta FM = \pm 0.005$  for 2-digit reporting. The standard deviation provides a guide to decide how many digits are appropriate to report. One can initially check that a representative problem remains bounded for many more revolutions, then return to the 2-rev criterion for generating the remainder of a data base. For this study, the SA-DES solutions used a 3-digit criterion whereas some of the SA-RANS solutions used a 2-digit criterion.

#### 4.4 Rotor Wake and AMR

The importance of spatial accuracy, turbulence model, and FM convergence have been previously discussed. The rotor wake is now refined using three OB-AMR resolutions, i.e.,  $\Delta_{wake} = 10\%$ ,  $5\%$ , and  $2.5\% c_{tip}$ , to establish OB grid convergence for the FM. Each case only uses level-1 grids in the rotor wake to resolve high-gradient regions without the need for interpolation, see Section 3.2. Moreover, NB-grids have a normal grid spacing at their outer boundaries of  $\Delta = 5\% c_{tip}$ , maintaining a factor of two grid spacing between NB-grids and their overlapping Cartesian OB-grids.

Figure 22 shows the instantaneous OB-AMR grids colored by vorticity magnitude and the total grid points (GP). The specified  $L_1$ -region and OB-AMR region are outlined with white lines. A time-dependent animation of the OB-AMR process shows that flow features leave the specified  $L_1$ -region and travel throughout the OB-AMR region with plenty of  $L_1$ -grid support. Equation 2 is used as the sensing function for all cases, requiring no adjustment of the default settings. One can observe the rapid grid growth with

wake-grid refinement. The finer AMR resolutions also result in larger coarse-grid regions due to the fine granularity of these OB-AMR grids.



a)  $\Delta_{\text{wake}}=10\%c_{\text{tip}}$ , 40 million GP.    b)  $\Delta_{\text{wake}}=5\%c_{\text{tip}}$ , 173 million GP.    c)  $\Delta_{\text{wake}}=2.5\%c_{\text{tip}}$ , 1.1 billion GP.

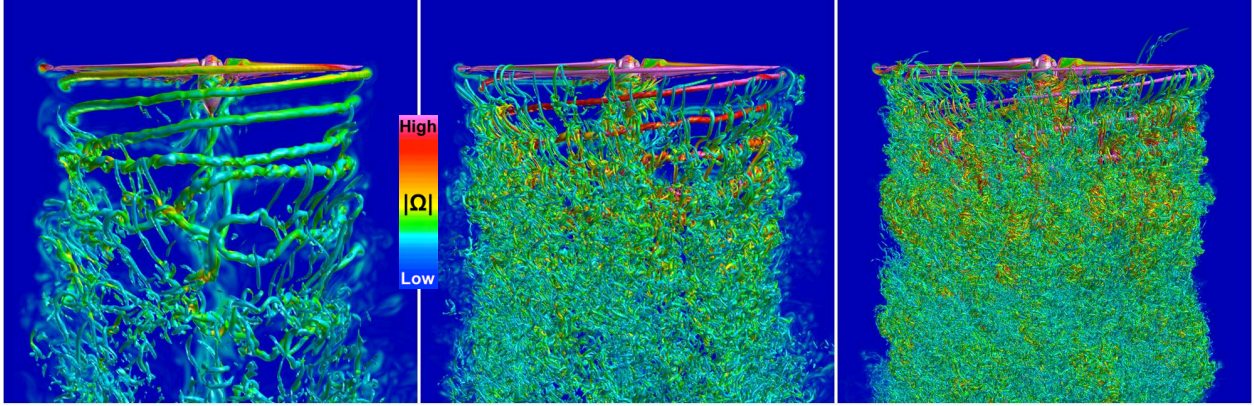
**Figure 22** OB-AMR Cartesian grids colored by vorticity magnitude,  $\theta=14^\circ$ .

The FM is summarized in Table 6 for each grid resolution in Fig. 22. Decreasing the grid spacing from  $10\%c_{\text{tip}}$  to  $5\%c_{\text{tip}}$  changes the FM by  $\Delta\text{FM}=0.005$ . This is a significant change, i.e., equivalent to the weight of one passenger. Further decreasing the grid spacing from  $5\%c_{\text{tip}}$  to  $2.5\%c_{\text{tip}}$  only changes the FM by 0.001. This change is not significant and indicates the OB-grids are grid-converged with respect to the FM. Chaderjian and Buning [4] originally reported  $\text{FM}=0.780$  using central differencing on the finest mesh whereas the HLLE++ upwind algorithm predicts  $\text{FM}=0.782$ . (The same NB grids were used.) The upwind results are within experimental error for all three wake-grid resolutions, see also Fig. 14. The FM from the  $10\%c_{\text{tip}}$  grid spacing differs from the final spatially converged FM ( $2.5\%c_{\text{tip}}$  spacing) by  $\Delta\text{FM}=0.006$ , or 0.77%. This seems like an acceptable compromise for doing trade studies at a reduced computational cost (grid size). However, the  $5\%c_{\text{tip}}$  grid spacing should be used for a final quantitative value. Moreover, Jia et al. [37] showed that a  $5\%c_{\text{tip}}$  resolution is needed for accurate acoustics with strong BVI. Using a  $10\%c_{\text{tip}}$  wake-grid spacing can introduce a 5dB error. The finest grid size of  $\Delta=2.5\%c_{\text{tip}}$  has about 1.1 billion grid points and is more suitable for a detailed study of vortex-wake turbulent structures and interactions.

$\Delta_{\text{wake}}$	$\text{FM}_{\text{DES}}$	$\Delta\text{FM}_{\text{EXP}}$	
$10\%c_{\text{tip}}$	0.776	-0.004	-0.51%
$5\%c_{\text{tip}}$	0.781	0.001	0.13%
$2.5\%c_{\text{tip}}$	0.782	0.002	0.26%

**Table 6** Effect of wake grid spacing on FM.

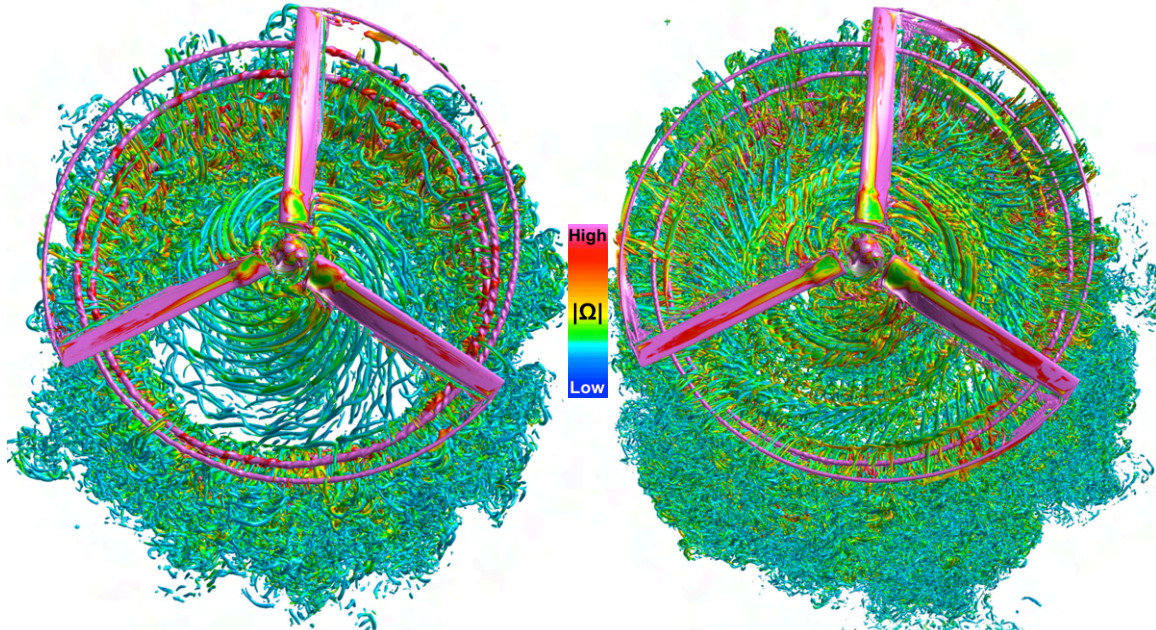
Figure 23 shows the development of the turbulent wake as the wake-grid is refined. Chaderjian et al. [4, 7] first identified these small vortical structures as “turbulent worms.” Others later reported seeing similar turbulent flow [9-11]. These instabilities naturally occur outside the turbulent boundary layer as LES-resolved flow when using hybrid RANS/LES turbulence models with adequate grid support. Notice more worms appear with grid refinement. Indeed, one should expect this progression with finer meshes, however, the larger worms do converge in number density and size through grid refinement.



a)  $\Delta_{\text{wake}}=10\%_{\text{ctip}}$ , FM=0.776.      b)  $\Delta_{\text{wake}}=5\%_{\text{ctip}}$ , FM=0.781.      c)  $\Delta_{\text{wake}}=2.5\%_{\text{ctip}}$ , FM=0.782.

**Figure 23** Rotor vortices, turbulent wake (q-criterion) and cutting plane colored by vorticity magnitude,  $\theta=14^\circ$ .

Figure 24 compares overhead views of the tip vortices and rotor wake using central differencing and the improved HLLE++ upwind algorithm. They look very similar, having tip vortices (both outboard and inboard) in good location agreement, a worm structure following along the vortex sheet, and nearly identical FM. However, there are two noticeable differences. The central scheme has fewer worms interior to the vortex sheet, and they appear somewhat larger in diameter than the upwind result. These differences suggest the central scheme is more dissipative than the upwind scheme, see Table 4, even though care was taken to reduce the artificial viscosity as far as practical while maintaining code stability [4, 7].



a) Central differences, FM=0.780 [4, 7].

b) HLLE++ upwind differences, FM=0.782.

**Figure 24** Overhead view of rotor vortices and wake (q-criterion), where  $\Delta_{\text{wake}}=2.5\%_{\text{ctip}}$ ,  $\theta=14^\circ$ .

This high-resolution flow was animated using the q-criterion by a post-processed ray-tracing algorithm, where the solution was saved to disk every degree, i.e., every 4<sup>th</sup> time step. This resulted in 61TB of data for one revolution. Figure 25 is a single frame from the animation, where the front portion of the flow is removed together with a bi-color spectrum to better see the interior vortex-wake details. The shear layers, which are confluent boundary layers leaving a rotor blade's trailing edge, form a helix as they descend downward, see also Gray's schematic in Fig. 10. These shear layers descend downward at a greater rate

( $V_{SL}$ ) than the tip-vortex helix. As the shear layers pass a vortex they are stretched and entrained into the vortex, forming a continuous s-shape along the vortex sheet. This vortex stretching process thins and elongates the vorticity within the shear layer forming worms that tightly wrap around the vortex cores. Gray [25] in 1956 was perhaps the first to give experimental evidence of worms, see Fig. 26, though he did not recognize them as such. However, Wolf et al. [12] recently provided the first definitive experimental proof of worms through an innovative use of tomo-PIV, see Fig. 27, and Schwarz et al. [31] carried out companion CFD simulations. They refer to the largest scales entrained into the vortices as “secondary vortices,” and conclude the CFD secondary vortices are of reasonable physical size. This is a suitable description of these larger vorticity-dominant flow structures. However, the term “worm” [4, 7] was originally used to describe LES instability of all sizes found in the turbulent wake, including secondary, tertiary, ... An example of a small-scale turbulent worm is identified in Fig. 25, and can be seen in experiment, i.e., Fig. 27. Turbulent worms seem to be a suitable name for all vortical scales in the rotor wake, especially the smaller ones.

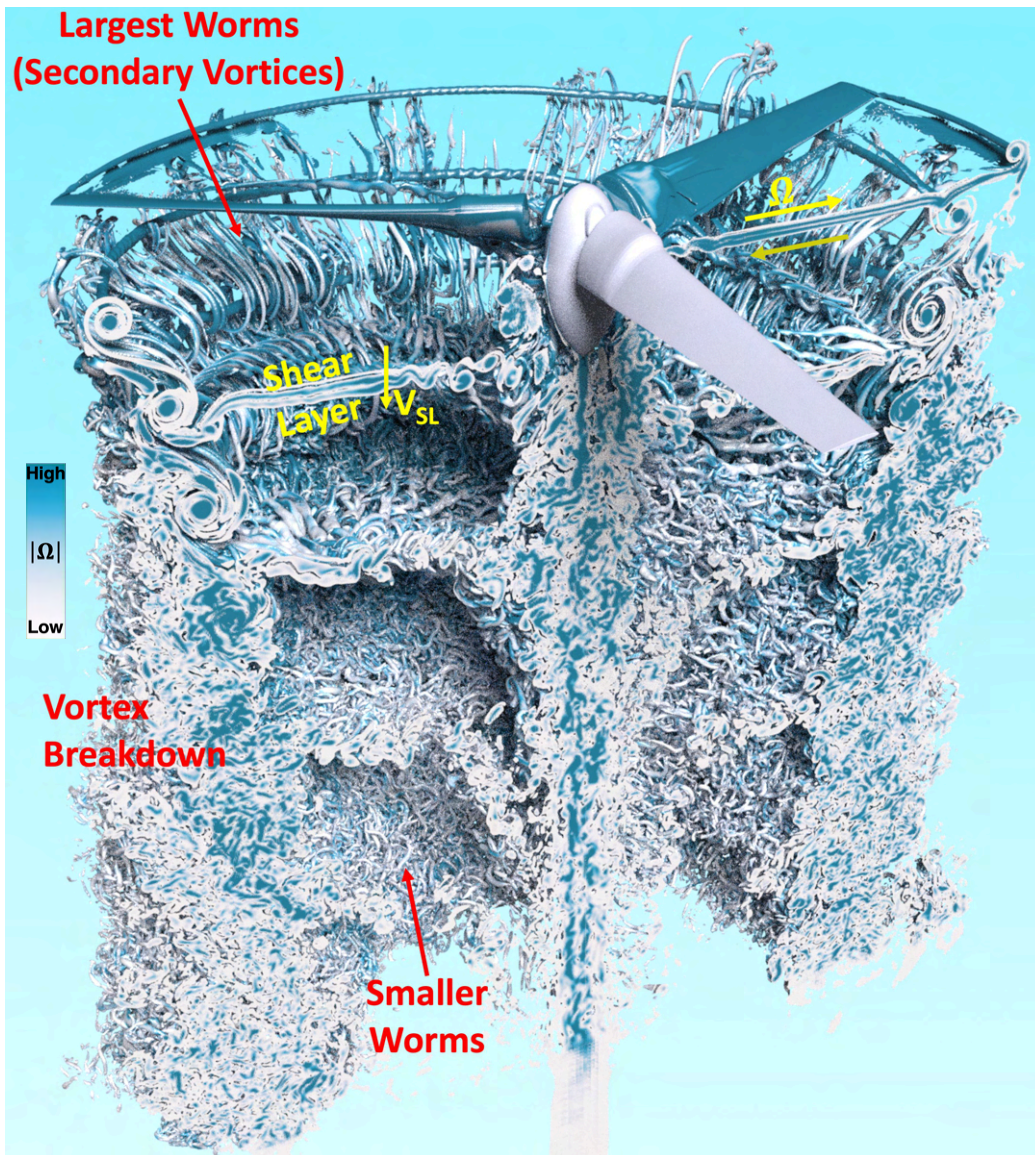


**Figure 25** Physics of the rotor wake. Cutaway view of the  $q$ -criterion colored by vorticity magnitude, SA-DES,  $\Delta_{wake}=2.5\%C_{tip}$ ,  $\theta=14^\circ$ .

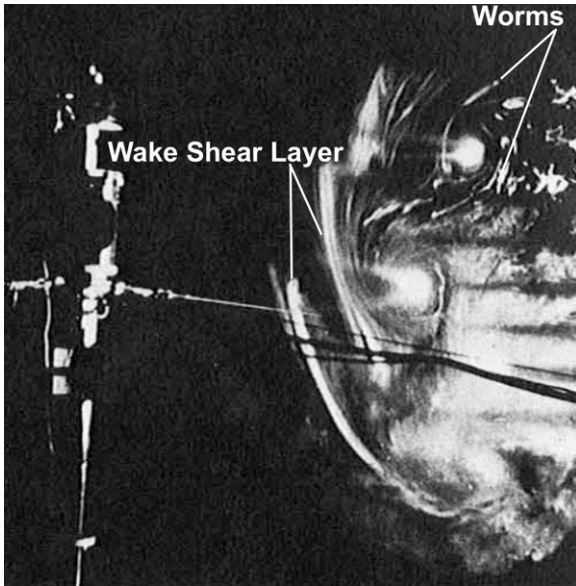


**Figure 26** Photo of Gray’s single-blade rotor experiment [25-26]. Smoke is used to visualize the vortex wake.

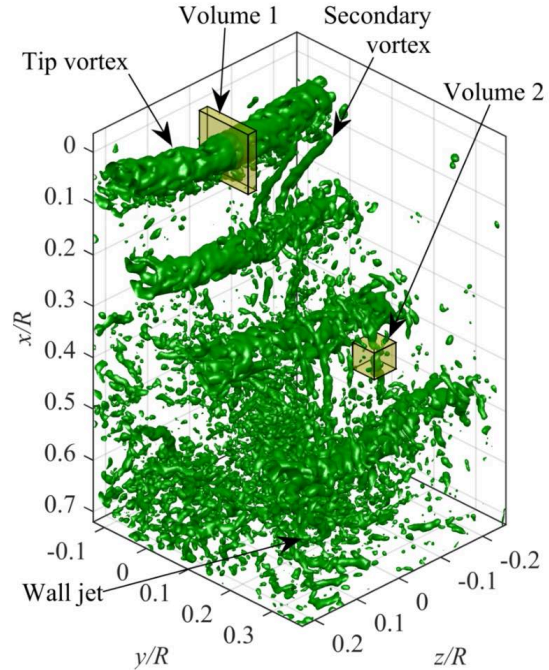
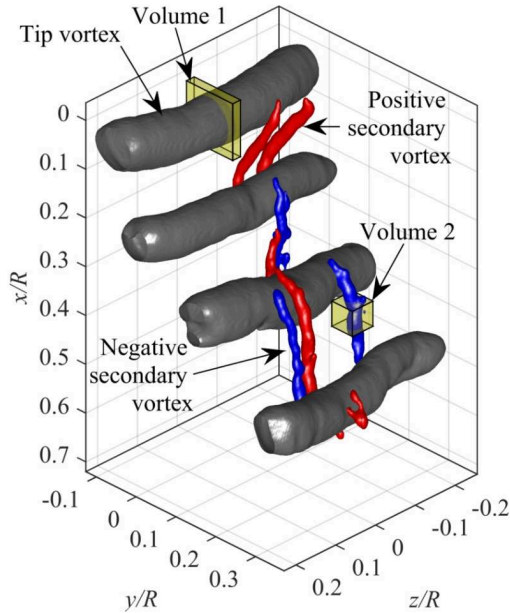


**Figure 27** Worms and secondary vortices observed in experiment using tomo-PIV [12].

The turbulent wake shown in Fig. 25 contains pockets of empty space. These gaps are the distance between the rotor’s shear-layer helix. In other words, the vortex wake is not uniformly filled with worms. Figures 23-24 can be misleading in this respect. Moreover, the density of worms increases farther below the rotor blades. This is because there are more shear-layer/vortex interactions in the lower wake. This is also why secondary vortices in the upper wake are more readily visible and fewer in number. The number of worms also increases with simulation time until a stable equilibrium is reached. One should also expect a higher density of worms as the number of blades is increased, providing more shear-layer/vortex interactions. All these phenomena are due to the interaction of vorticity containing shear layers being stretched and entrained into the tip-vortex helix.

The secondary vortices have been observed both in experiment [12] (see Figs. 27-28) and CFD [38] to develop vortex pairs with an alternating sense of rotation. This should be expected because the boundary layers leaving the blade trailing edge form a confluent boundary layer (shear layer) with an opposite sense of rotation from the upper and lower blade surfaces, see right side of Fig. 25. As the shear layer is stretched and entrained into the primary vortices, the resulting secondary vortices will also tend to form pairs of opposite spin, see Fig. 29. Figure 29 also indicates an equal distribution of worms with opposite spin.

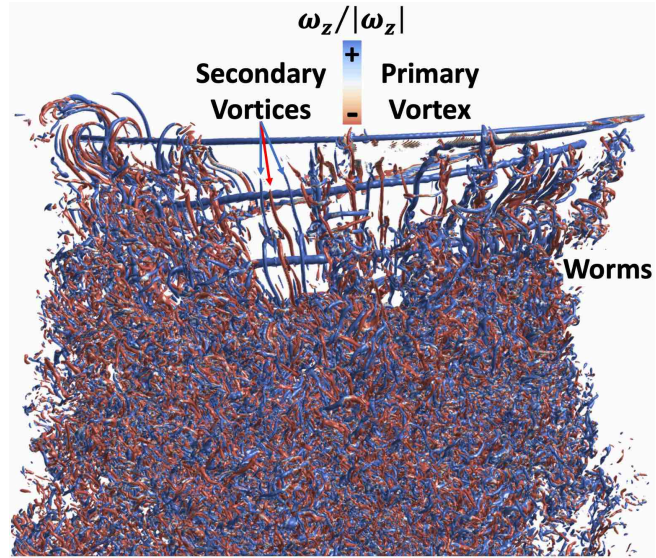
Figure 25 also exhibits primary vortex breakdown. Recall that improvements to the HLLC++ algorithm have resulted in an implicit and temporally converged solution, including the subiteration update of the overset boundary conditions. This breakdown is probably due to the strong tip vortices caused by a high-twist propeller. It would be useful to investigate, both with CFD and experiment, the vortex core strength as a function of wake age to determine if blade twist is the root cause of the breakdown. Vortex breakdown tends to occur about 75%R below the TRAM rotor blades. The LES mode of SA-DES may also be reducing the TEV too much. This would produce too many worms that encircle and weaken the tip vortices. It would be useful to compare the Reynolds stresses found in experiment with the SA-DES rotor simulation.



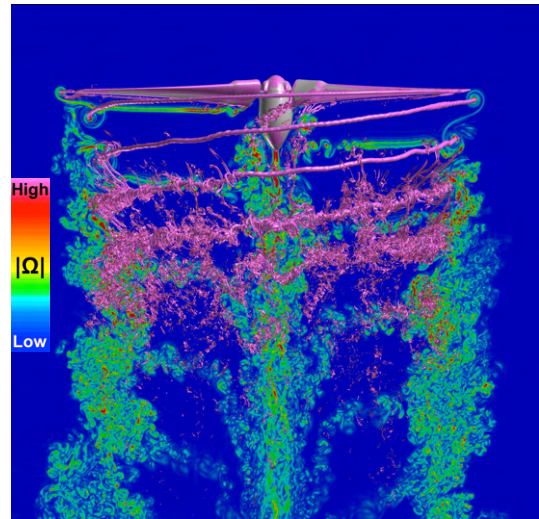
**Figure 28** Primary and secondary vortices observed in experiment [12]. Red and blue have opposite spin.

Figure 30 shows the blade-tip vortices and a cutting plane colored by vorticity magnitude. However, in this figure worms of all scales have been filtered out by adjusting a threshold to exclude iso-surfaces of the  $q$ -criterion with low vorticity. In this way the tip vortices can be more readily seen. There are two advantages to generating a filtered image. First, the vortex breakdown can be clearly seen. Note that even after breakdown, some semblance of a vortex core remains intact as a swirling mass of fluid. Eventually the vortex breaks up into smaller turbulent structures. Second, an overhead view of the tip vortices provides a means to measure vortex core diameter with wake age. Care was taken to select a  $q$ -criterion iso-surface value to get the correct vortex core size. This was accomplished at a wake age of  $\psi=30^\circ$ , where the vortex core diameter matched the distance between the core's peak crossflow velocities. The core diameter is not very sensitive to the iso-surface value.

Figure 31 shows the normalized vortex-core diameter variation with wake age for different OB wake-grid resolutions. Data from several experiments [39-41] are also included in the figure. The coarsest mesh,  $\Delta_{\text{wake}}=10\%c_{\text{tip}}$ , has a CFD vortex core that is about three times the size of the physical core. Refining the mesh to  $\Delta_{\text{wake}}=5\%c_{\text{tip}}$  reduces the size of the vortex core almost by half. The finest mesh,  $\Delta_{\text{wake}}=2.5\%c_{\text{tip}}$ , goes through the scatter of experimental data. Note that the same wake-grid resolution for the central scheme still has a diffused vortex core. Table 7 provides a quantitative comparison of vortex core diameter



**Figure 29** Closeup of primary and secondary vortices computed using the HLLE++ algorithm, SA-DES,  $\Delta_{\text{wake}}=2.5\%c_{\text{tip}}$ ,  $\theta=14^\circ$ . Red/blue indicate opposite spin.



**Figure 30** High-pass vorticity filter applied to  $q$ -criterion. SA-DES,  $\Delta_{\text{wake}}=2.5\%c_{\text{tip}}$ ,  $\theta=14^\circ$ .

with experiment at a wake age of  $\psi=10^\circ$ . The HLLE++ upwind algorithm matches the experiment on the finest mesh while the central difference algorithm still has a diffused vortex core that is 42% too large. This demonstrates the low-diffusion property of the upwind algorithm.

Figure 32 shows a top view of a blade tip vortex where the vortex core has a physically correct size. One can see the formation of the tip vortex as the upper and lower blade boundary layers form a braid, see Fig. 32 insert. Therefore the comparison was made at  $\psi=10^\circ$ , where the vortex core had time to form.

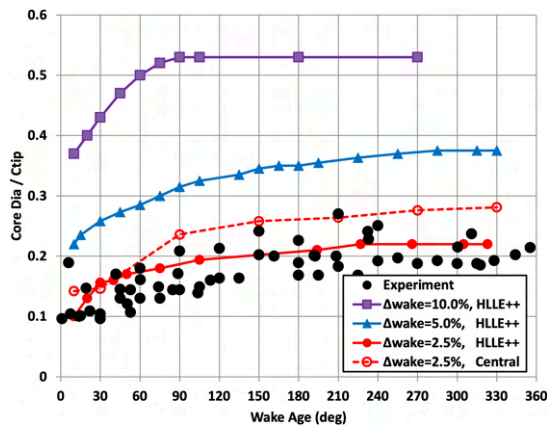


**Figure 31** Vortex core growth with wake age. SA-DES,  $\theta=14^\circ$ .

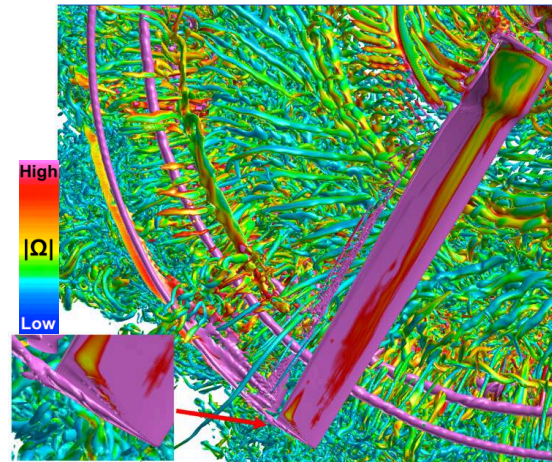


**Figure 32** Closeup of tip vortex (q-criterion). SA-DES,  $\Delta_{\text{wake}}=2.5\%c_{\text{tip}}$ ,  $\theta=14^\circ$ .

Method	$\Delta_{\text{wake}}$	Core Dia/Ctip	Difference
Exp	NA	0.100	NA
HLLE++	10.0% $c_{\text{tip}}$	0.370	270%
HLLE++	5.0% $c_{\text{tip}}$	0.220	120%
HLLE++	2.5% $c_{\text{tip}}$	0.100	0%
Central	2.5% $c_{\text{tip}}$	0.142	42%

**Table 7** Vortex core diameter at wake age of  $\psi=10^\circ$ ,  $\theta=14^\circ$ .

## 5. Conclusions

Time-dependent fully-turbulent RANS and DES simulations using the OVERFLOW CFD code for an isolated V22 (TRAM) rotor in hover have been carried out using the Spalart-Allmaras turbulence model and an improved low-diffusion HLLE++ upwind algorithm with SSOR. Emphasis has been placed on lessons learned over the past decade regarding the effects of high-order spatial differences, body-grid resolution, detached eddy simulation, and refinement of the rotor wake on predicting the FM. The physics of a highly refined rotor wake with a high degree of LES instability, i.e., worms of various size, was also discussed. Second-order time accuracy was used throughout with a dual-time subiteration convergence that exceeded 2-orders or magnitude.

- The CFD FM agreed with experiment and within experimental error over a range of collectives and wake-grid resolutions, typically 0.1-0.5%. The experiment's measurement error was  $\Delta_{\text{FM}}=\pm 0.005$ , i.e., equivalent to the weight of one UAM passenger.
- Four key factors were important to accurately predict the FM.
  - Fifth-order spatial differencing significantly improved the FM over the 3<sup>rd</sup>-order option.

- The SA-DES turbulence model provided the greatest improvement. The SA-RANS model was often inaccurate and slow to converge, especially at the lower collective.
- The FM must be fully converged, to the 3<sup>rd</sup>-digit when possible.
- Refining the rotor wake resulted in a minor improvement to the FM. Cartesian OB-AMR resolution varied from  $\Delta S_{\text{wake}}=10\%$ ,  $5\%$ , and  $2.5\%c_{\text{tip}}$ .
- The running mean FM was used to statistically determine the FM and when it was converged.
  - The standard deviation provides guidance on whether it is meaningful to report FM with two or three significant figures. All SA-DES cases justified a 3-digit FM whereas some SA-RANS cases could only report a 2-digit FM.
  - A general quick-start procedure is developed that reduces the computational work of a hover simulation five-fold, to that of forward flight. This procedure was demonstrated for the TRAM rotor in free air, and previously for a rotor in a test facility [33].
- Refining the rotor wake using OB-AMR and the SA-DES turbulence model produced LES instability (worms) predicted computationally more than a decade ago, and recently observed in a separate DLR experiment [12].
  - The term “turbulent worms” was originally used to describe the range of observed LES scales, although secondary vortices [12, 31] seem to be a preferred term describing the largest worms surrounding the tip vortices.
  - The blade trailing-edge shear layer forms a helix that descends downward at a faster rate than the blade-tip vortices. As a shear layer passes a vortex, it is stretched and entrained into a vortex forming an s-shaped pattern. This vortex-stretching process creates the secondary vortices and smaller worms.
  - Experiment first reported the secondary vortices tend to occur in pairs of opposite spin. This was also previously observed with CFD [38] and the current simulations. CFD animations indicate their origin can be traced to the confluent boundary layers leaving the blade trailing edge, which form the shear-layer helix in the wake. These shear layers contain vorticity of opposite spin that originated from the upper and lower blade surfaces.
  - A wake grid resolution of  $\Delta S_{\text{wake}}=2.5\%c_{\text{tip}}$  produced vortices of correct physical size. This is an improvement over the original central difference scheme used a decade ago [4, 7]. The HLLE++ upwind algorithm has lower diffusion than the central scheme.
  - There are significant pockets of empty space in between the wake shear layers, i.e., the vortex wake is not uniformly filled with worms.
  - The physics of creating worms in the rotor wake imply the following:
    - Increasing the number of rotor blades produces more worms due to the greater number of vortex/shear-layer interactions.
    - The worms develop and grow in number with time from impulsive start, but eventually reach equilibrium once the vortex/shear-layer interactions are established.
    - Finer wake-grid resolution produces smaller worms. However, the larger worms, e.g., secondary vortices, should converge in size with grid refinement.
    - Vortex breakdown provides additional vorticity to form smaller worms.
- The following are recommended to accurately predict FM in fully turbulent flow:
  - HLLE++/SSOR algorithm with 5<sup>th</sup>-order upwind differencing.
  - SA-DES turbulence model with the SARC rotation/curvature correction.

- Tightly converge the running mean FM using the quick-start procedure.
- Trade studies can be efficiently carried out within 1% FM error using  $\Delta S_{\text{wake}}=10\%c_{\text{tip}}$ .
- Final quantitative FM analysis and acoustics [37] should use  $\Delta S_{\text{wake}}=5\%c_{\text{tip}}$ , which for the TRAM resulted in a 0.13% FM error, i.e.,  $\Delta FM=0.001$ .
- A wake-grid spacing of  $\Delta S_{\text{wake}}=2.5\%c_{\text{tip}}$  can be used to study the tip vortices and their interactions with correct physical size, vortex breakdown, secondary vortices, and smaller scale worms.
- Flow visualization can remove the worms to better view the tip vortices. This is accomplished using a high-pass filter that restricts the image to higher vorticity values.
- Future work could explore the following questions:
  - What are the precise details of some rotor flows that lead to early vortex breakdown?
  - Does the SA-DES turbulence model reduce the TEV in the rotor wake too much? A side-by-side comparison of CFD and experiment Reynolds stresses could help answer this question.

## Acknowledgements

The author would like to thank the following:

- NASA’s Revolutionary Vertical Lift Technology Project (RVLT) for supporting this work for more than a decade.
- Drs. Pieter Buning and Joe Derlaga at NASA Langley Research Center for their many helpful discussions about the OVERFLOW CFD code and numerical algorithms.
- Mr. Timothy Sandstrom at the NAS Visualization & Data Analysis Group at NASA Ames Research Center. His tireless efforts, incredible visualization expertise, and innovation have greatly enhanced my understanding of these time-dependent flows.

## References

- [1] Yamauchi, G. K., and Young, L. A., “A status of NASA Rotorcraft Research,” NASA/TP-2009-215369.
- [2] Lee-Rausch, E. M., and Biedron, R. T., “Simulation of an Isolated Tiltrotor in Hover With an Unstructured Overset-Grid RANS Solver,” American Helicopter Society 65<sup>th</sup> Annual Forum Proceedings, Grapevine, TX, May 27-29, 2009.
- [3] Wissink, A. M., Kamkar, S., Pulliam, T. H., Sitaraman, J., and Sankaran, V., “Cartesian Adaptive Mesh Refinement for Rotorcraft Wake Resolution,” AIAA 2010-4554, July 2010. [doi.org: 10.2514/6.2010-4554](https://doi.org/10.2514/6.2010-4554)
- [4] Chaderjian, N. M., and Buning, P. G., “High Resolution Navier-Stokes Simulation of Rotor Wakes,” Proceedings of the American Helicopter Society 67<sup>th</sup> Annual Forum, Virginia Beach, VA, May 3-5, 2011.
- [5] Swanson, S. M., McCluer, M. S., Yamauchi, G. K., and Swanson, A. A., “Airloads Measurements from a ¼-Scale Tiltrotor Wind Tunnel Test,” 25<sup>th</sup> European Rotorcraft Forum, Rome, Italy, September 1999.
- [6] Johnson, J. L., and Young, L. A., “Tilt Rotor Aeroacoustic Model Project,” Confederation of European Aerospace Societies (CEAS) Forum on Aeroacoustics of Rotorcraft and Propellers, Rome, Italy, June 1999.
- [7] Chaderjian, N. M., “Advances in Rotor Performance and Turbulent Wake Simulation using DES and Adaptive Mesh Refinement,” Paper Number ICCFD7-3506, July 2012., [www.iccfd.org/iccfd7/assets/pdf/papers/ICCFD7-3506\\_paper.pdf](http://www.iccfd.org/iccfd7/assets/pdf/papers/ICCFD7-3506_paper.pdf).

- [8] Hariharan, N. S., Egolf, T. A., and Sankar, L. N., "Simulation of Rotor in Hover: Current State and Challenges," Paper AIAA 2014-0041, 52nd Aerospace Sciences Meeting, National Harbor, MD, USA, January 13–17, 2014. doi: [10.2514/6.2014-0041](https://doi.org/10.2514/6.2014-0041)
- [9] Potsdam, M., and Jayaraman, B., "UH-60A Rotor Tip Vortex Prediction and Comparison to Full-Scale Wind Tunnel Measurements," American Helicopter Society 70th Annual Forum, Montreal, Canada, May 20–22, 2014.
- [10] Jain, R., "A Comparison of CFD Hover Predictions for the Sikorsky S-76 Rotor," Paper AIAA 2016-0032, AIAA Science and Technology Forum and Exposition, San Diego, CA, USA, January 4–8, 2016. doi: [10.2514/6.2016-0032](https://doi.org/10.2514/6.2016-0032)
- [11] Öhrle, C., Schäferlein, U., Keßler, M., and Krämer, E., "Higher-order Simulations of a Compound Helicopter using Adaptive Mesh Refinement," American Helicopter Society 74th Annual Forum, Phoenix, AZ, USA, May 15–17, 2018.
- [12] Wolf, C. C., Schwarz, C., Kaufmann, K., Gardner, A. D., Michaelis, D., Bosbach, J., Schanz, D., and Schröder, A., "Experimental study of secondary vortex structures in a rotor wake," *Experiments in Fluids*, Vol. 60, (175), 2019. doi: [10.1007/s00348-019-2807-1](https://doi.org/10.1007/s00348-019-2807-1)
- [13] Derlaga, J. M., Jackson, C. W., and Buning, P. G., "Recent Progress in OVERFLOW Convergence Improvements," AIAA 2020-1045, Jan. 2020. doi: [10.2514/6.2020-1045](https://doi.org/10.2514/6.2020-1045)
- [14] Nichols, R. H., and Buning, P. G., "User's Manual for OVERFLOW 2.3," NASA Langley Research Center, Hampton, VA, Jan. 2022. <https://overflow.larc.nasa.gov/>
- [15] Buning, P. G., and Pulliam, T. H., "Cartesian Off-Body Grid Adaption for Viscous Time-Accurate Flow Simulations," AIAA-2011-3693, June 2011. doi: [10.2514/6.2011-3693](https://doi.org/10.2514/6.2011-3693)
- [16] Yoon, S., Pulliam, T.H., and Chaderjian, N.M., "Simulations of XV-15 Rotor Flows in Hover Using OVERFLOW," 5<sup>th</sup> Decennial AHS Aeromechanics Specialists' Conference, San Francisco, CA, January 2014.
- [17] Chaderjian, N. M., "Numerical Simulation of Dynamic Stall Using Near-Body Adaptive Mesh Refinement," Paper Number ICCFD10-102, July 9-13, 2018. [www.iccfd.org/iccfd10/papers/ICCFD10-102-Paper.pdf](http://www.iccfd.org/iccfd10/papers/ICCFD10-102-Paper.pdf)
- [18] Buning, P. G., and Pulliam, T. H., "Near-Body Grid Adaption for Overset Grids," AIAA-2016-3326, June 2016. doi: [10.2514/6.2016-3326](https://doi.org/10.2514/6.2016-3326)
- [19] Pulliam, T. H., and Steger, J. L., "Implicit Finite-Difference Simulations of Three-Dimensional Compressible Flow," *AIAA Journal*, Vol. 18, No. 2, 1980, pp. 159–167. doi: [10.2514/3.50745](https://doi.org/10.2514/3.50745).
- [20] Pulliam, T. H., and Chaussee, D. S., "A Diagonal Form of an Implicit Approximate-Factorization Algorithm," *Journal of Computational Physics*, Vol. 39, No. 2, 1981, pp. 347-363.
- [21] Tramel, R. W., Nichols, R. H., and Buning, P. G., "Addition of Improved Shock-Capturing Schemes to OVERFLOW 2.1," AIAA-2009-3988, June 2009. doi: [10.2514/6.2009-3988](https://doi.org/10.2514/6.2009-3988).
- [22] Nichols, R. H., Tramel, R. W., and Buning, P. G., "Solver and Turbulence Model Upgrades to OVERFLOW 2 for Unsteady and High-Speed Applications," AIAA-2006-2824, June 2006. doi: [10.2514/6.2006-2824](https://doi.org/10.2514/6.2006-2824)
- [23] Spalart, P. R., and Allmaras, S. R., "A One-Equation Turbulence Model for Aerodynamic Flows," AIAA-92-0439, January 1992. doi: [10.2514/6.1992-439](https://doi.org/10.2514/6.1992-439)
- [24] Ramasamy, M., Johnson, B., and Leishman, J. G., "Turbulent Tip Vortex Measurements Using Dual-Plane Digital Particle Image Velocimetry," Proceedings of the American Helicopter Society 64<sup>th</sup> Annual Forum, Montréal, Canada, April 29-May 1, 2008. doi: [10.2514/1.39202](https://doi.org/10.2514/1.39202)
- [25] Gray, R. B., "An Aerodynamic Analysis of a Single-Bladed Rotor in Hovering and Low-Speed Forward Flight as Determined from Smoke Studies of the Vorticity Distribution in the Wake," Princeton University A.E. Dept. Report No. 356, 1956.
- [26] Gray, R. B., "Vortex Modeling for Rotor Aerodynamics," The 1991 Alexander A. Nikolsky Lecture presented at the American Helicopter Society 47<sup>th</sup> Annual Forum, Phoenix, AZ, May 1991.
- [27] Shur, M. L., Strelets, M. K., Travin, A. K., and Spalart, P. R., "Turbulence Modeling in Rotating and Curved Channels: Assessing the Spalart-Shur Correction," *AIAA Journal*, Vol. 38, No. 5, May 2000, pp. 784-792. doi: [10.2514/2.1058](https://doi.org/10.2514/2.1058)

- [28] Smagorinsky, J., "General Circulation Experiments with the Primitive Equations. I. The Basic Experiment," *Monthly Weather Review*, Vol. 91, No. 3, pp. 99-164. doi: [10.1175/1520-0493\(1963\)091<0099:GCEWTP>2.3.CO;2](https://doi.org/10.1175/1520-0493(1963)091<0099:GCEWTP>2.3.CO;2)
- [29] Spalart, P., Jou, W-H., Strelets, M., and Allmaras, S. "Comments on the Feasibility of LES for Wings and on a Hybrid RANS/LES Approach," First AFOSR Conference on DNS/LES, August 1997, Greyden Press, Columbus, OH.
- [30] Spalart, P. R., Deck, S., Sur, M. L., Squires, K. D., Strelets, M., and Travin, A., "A New Version of Detached-Eddy Simulation, Resistant to Ambiguous Grid Densities," *Theoretical and Computational Fluid Dynamics (2006)*, Vol. 20, No. 3, pp. 181-195. doi: [10.1007/s00162-006-0015-0](https://doi.org/10.1007/s00162-006-0015-0)
- [31] Schwarz, C., Andrew, A., Wolf, C. C., Brinkema, R., Potsdam, M., and Gardner, A. D., "Development of Secondary Vortex Structures in Rotor Wakes," Vertical Flight Society's 77<sup>th</sup> Annual Forum, Virtual, May 10-14, 2021. doi: [10.1007/s00348-021-03348-8](https://doi.org/10.1007/s00348-021-03348-8).
- [32] Ahmad, J. U., Yamauchi, G. K., and Kao, D. L., "Comparison of Computed and Measured Vortex Evolution for a UH-6A Rotor in Forward Flight," AIAA 2013-3160, June 2013. doi: [10.2514/6.2013-3160](https://doi.org/10.2514/6.2013-3160)
- [33] Chaderjian, N. M., and Ahmad, J. U., "Navier-Stokes Assessment of Test Facility Effects on Hover Performance," Proceedings of the American Helicopter Society 71<sup>st</sup> Annual Forum, Virginia Beach, VA, May 5-7, 2015.
- [34] Srinivasan, Ganapathi R., "A Free-Wake Euler and Navier-Stokes CFD Method and its Application to Helicopter Rotors Including Dynamic Stall," JAI Associates, Inc. Technical Report 93-01, November 1993.
- [35] Repsher, S. J., and Spalart, P. R., "A Far Field Boundary and Initial Condition for the Simulation of Hovering Rotors based on Turbulent Jets," American Helicopter Society 69<sup>th</sup> Annual Forum, Phoenix, AR, May 21-23, 2013.
- [36] Spalart, P. R., "On the flow field induced by a hovering rotor or a static jet," *Journal of Fluid Mechanics (2012)*, Vol. 701, pp. 473-481. doi: [10.1017/jfm.2012.188](https://doi.org/10.1017/jfm.2012.188)
- [37] Jia, Z., Lee, S., and Brentner, K. S., "Assessment of Turbulence Modeling and Wake-Grid Resolution for Lift-Offset Coaxial Rotor Simulations," AIAA-2018-4120, Atlanta, GA, June 25-29, 2018. doi: [10.2514/6.2018-4120](https://doi.org/10.2514/6.2018-4120).
- [38] Bodling, A., and Potsdam, M., "Numerical Investigation of Secondary Vortex Structures in a Rotor Wake," Vertical Flight Society's 75th Annual Forum, Virtual, October 5-8, 2020
- [39] Leishman, J. G., and Bagai, A., "Challenges in Understanding the Vortex Dynamics of Helicopter Rotor Wakes," *AIAA Journal*, Vol. 36, July 1998, pp. 1130-1140. doi: [10.2514/2.510](https://doi.org/10.2514/2.510).
- [40] McAlister K., and Heineck, J., "Measurements of the Early Development of Trailing Vorticity From a Rotor," NASA/TP-2002-211848, AFDD/TR-02-A001, May 2002.
- [41] Ramasamy, M., Johnson, B., and Leishman, J. G., "Understanding the Aerodynamic Efficiency of a Hovering Micro-Rotor," *Journal of the American Helicopter Society*, Vol 53, (4), October 2008, pp. 412-428. doi: [10.4050/JAHS.53.412](https://doi.org/10.4050/JAHS.53.412).